International Journal of Biological Macromolecules 330 (2025) 148124

Contents lists available at ScienceDirect

International Journal of Biological Macromolecules

journal homepage: www.elsevier.com/locate/ijbiomac

Structural perspective on the design of selective DYRK1B inhibitors

Przemyslaw Grygier [a,b], Katarzyna Pustelny [a,c,1], Filipe Menezes [d,1], Malgorzata Jemiola-Rzeminska [e], Piotr Suder [f], Grzegorz Dubin [a], Anna Czarna [a,*]

[a] Malopolska Centre of Biotechnology, Jagiellonian University, Gronostajowa 7a, 30-387, Krakow, Poland
[b] Doctoral School of Exact and Natural Sciences, Jagiellonian University, Prof. St. Lojasiewicza 11, 30-348, Krakow, Poland
[c] Department of Physical Biochemistry, Faculty of Biochemistry, Biophysics and Biotechnology, Jagiellonian University, Gronostajowa 7, 30-387, Krakow, Poland
[d] Helmholtz Munich, Molecular Targets and Therapeutics Center, Institute of Structural Biology, Ingolstädter Landstr. 1, 85764, Neuherberg, Germany
[e] Department of Plant Physiology and Biochemistry, Faculty of Biochemistry, Biophysics and Biotechnology, Jagiellonian University, Gronostajowa 7, 30-387, Krakow, Poland
[f] Department of Analytical Chemistry and Biochemistry, Faculty of Materials Science and Ceramics, AGH University Cracow, A. Mickiewicza 30, 30-059, Krakow, Poland

ARTICLE INFO

Keywords:
DYRK1B
X-ray crystallography
Quantum mechanical analysis

ABSTRACT

Dual-specificity tyrosine-phosphorylation-regulated kinase 1B (DYRK1B) has recently emerged as a critical therapeutic target in oncology and non-alcoholic fatty liver disease. As a kinase, DYRK1B plays key roles in regulating cellular survival pathways; however, the lack of structural information has impeded the development of selective inhibitors. In this study, we implemented multi-method framework: recombinant expression and stability profiling, cellular target engagement, enzyme inhibition, biophysical thermodynamics, cell-based pathway readout, X-ray crystallography, quantum-mechanical and molecular-dynamics analyses. We report the crystal structure of DYRK1B in complex with the small-molecule inhibitor AZ191. For comparative purposes, we also present the structure of the closely related kinase, DYRK1A, bound to the same ligand. While a structural overlay of the two kinase domains reveals overall negligible differences, detailed inspection highlights distinct features within the hinge-binding region of DYRK1B that are pivotal for achieving kinase selectivity. Moreover, detailed evaluation of the active site architecture reveals a notable difference in the accessibility of the catalytic lysine residue between DYRK1B and DYRK1A, suggesting potential strategies to distinguish selective binders. Overall, these findings provide important macromolecular insights into the DYRK1B structure and offer a structural framework to guide medicinal chemistry efforts towards improved inhibitor selectivity with minimized off-target activity.

1. Introduction

Protein phosphorylation is the most widespread post-translational modification facilitating cellular signal transduction [1]. Deregulation of kinase signaling underlies multiple human diseases. However, one of the challenges in exploring phosphorylation as a drug target arises in designing selective inhibitors addressing over 500 protein kinases of the human kinome [2,3]. Within this landscape, the dual-specificity tyrosine phosphorylation-regulated kinases (DYRKs) have emerged as critical targets. DYRKs belong to a family of CMGC kinases, which includes cyclin-dependent kinases (C), mitogen-activated protein kinases (M), glycogen synthase kinases (G), and CDC-like kinases (C). The uniqueness of DYRKs is their ability to autophosphorylate on tyrosine residues while phosphorylating other substrates exclusively on serine and threonine [4–6]. Within the DYRK family, the two closely related paralogs, DYRK1A and DYRK1B, are of major interest as drug targets due to their multifaceted and often distinct roles in cellular processes that are dysregulated in various diseases.

The need to study DYRK1A and DYRK1B, both individually and together, is underscored by their diverse pathological associations. DYRK1A, with its gene located at the Down Syndrome Critical Region (DSCR) of chromosome 21, is widely considered a key drug target in neurological disorders, including Down Syndrome (DS), Alzheimer's, and Parkinson's disease [7–10]. This neurological link is further

* Corresponding author at: Malopolska Centre of Biotechnology, Jagiellonian University, 30-387, Krakow, Poland.
E-mail address: anna1.czarna@uj.edu.pl (A. Czarna).
[1] These authors contributed equally.

https://doi.org/10.1016/j.ijbiomac.2025.148124
Received 5 May 2025; Received in revised form 3 October 2025; Accepted 4 October 2025
Available online 6 October 2025

supported by structural features unique to DYRK1A; it possesses a histidine-rich region (HRD) for localization to nuclear speckles that is absent in DYRK1B [11]. In contrast, DYRK1B (MIRK) maps to chromosome 19, a region frequently amplified across several solid tumors (notably pancreatic and ovarian cancers) [12,13] aligning DYRK1B more directly with oncogenic programs.

Specifically, DYRK1B has emerged as a critical driver in several aggressive malignancies [14]. It is overexpressed in over 60 % of pancreatic ductal adenocarcinomas (PDAC), where it promotes a quiescent state that confers resistance to standard-of-care chemotherapies [15]. This trend of high protein expression despite a seemingly anti-proliferative function is observed across multiple malignancies. Elevated DYRK1B levels is also common beyond pancreas – reported in 41–60 % of ovarian cancers [16–18], and nearly 90 % of non-small-cell lung cancers [19]. DYRK1B protein is highly overexpressed in breast cancer (100 % in one cohort) and correlates with poor prognosis, despite a low gene amplification rate [20]. Furthermore, the mechanism driving this overexpression does not appear to be primarily genetic amplification. Roughly 10 % of pancreatic cancers harbor an amplification of the DYRK1B gene, a modest figure that is consistent with rates in ovarian (10 %), lung (4 %), and breast (2 %) tumors [14]. The presence of DYRK1B protein is also high, detected in 89 % of pancreatic tumors and 76 % of rhabdomyosarcomas [21,22]. Data from cancer cell lines further support its high expression, with elevated levels observed in 63 % of ovarian and 68 % of lung cancer lines [17,19]. Collectively, these observations reveal that high DYRK1B protein abundance is a recurrent feature across aggressive tumors, driven predominantly by non-genetic mechanisms (transcriptional upregulation or enhanced protein stability), with focal gene amplification contributing in a subset.

In these cancers, DYRK1B overexpression maintains cellular quiescence [15] and enhances cell survival by reducing reactive oxygen species (ROS) levels [23]. Consequently, genetic depletion or inhibition of DYRK1B leads to cell cycle re-entry and apoptosis, making it an attractive therapeutic strategy [24,25]. Therefore, patients with DYRK1B-overexpressing malignancies, such as certain pancreatic and ovarian cancers, would be the primary beneficiaries of selective DYRK1B inhibitors. Furthermore, both kinases are pivotal for human beta cell regeneration, with their inhibition showing promise in treating diabetes by promoting beta cell proliferation [7,26–28]. While DYRK1B silencing alone has a minimal effect on beta-cell proliferation, simultaneous silencing of DYRK1A and 1B results in significantly higher proliferation rates than silencing DYRK1A alone, suggesting that dual inhibitors also have therapeutic applications [29]. This complex interplay necessitates the development of both selective and dual inhibitors to dissect their individual functions and therapeutically target them effectively.

The current therapeutic landscape for targeting DYRK kinases is defined by a central limitation: a lack of inhibitor selectivity. This fundamental challenge is a primary reason why no DYRK1A or DYRK1B inhibitor has yet been approved for clinical use. Harmine, a β-carboline alkaloid, is the most common inhibitor used in preclinical studies to investigate the roles of DYRK1A and 1B [26,30,31]. However, harmine inhibits both kinases with comparable potency, which prevents the attribution of observed effects to a single paralog and poses a risk of off-target effects in a clinical setting [32]. While various other inhibitors have been reported, achieving high selectivity remains a major challenge due to the high degree of conservation within the ATP-binding pocket of the DYRK1A and DYRK1B catalytic domains. This structural similarity is the primary obstacle to developing paralog-specific drugs.

To overcome this challenge, a detailed structural understanding of the kinase domain is essential. Key features defining the active site include a glycine-rich loop, a DFG motif involved in ATP binding, and a gatekeeper residue (phenylalanine) guarding access to a hydrophobic back pocket [33–35]. The DFG motif adopts an “in” conformation in active kinases where the aspartic acid residue coordinates a $Mg^{2}+$ ion bound to the β- and γ- phosphate groups of ATP. Additionally, the activation loop contains the signature Tyr-Xxx-Tyr motif, which determines kinase activity through autophosphorylation (Fig. 1) [36].

The catalytic domain is flanked at the N-terminus by the DYRK homology box (DH), vital for autophosphorylation [6,37], and at the C-terminus by a PEST sequence promoting rapid degradation [38] (Fig. 1). While these features are highly conserved between DYRK1A and DYRK1B, the lack of a DYRK1B crystal structure has been a major barrier to exploiting any subtle differences**.** To address this, we chose AZ191 as a reference compound - a potent, ATP-competitive inhibitor of both DYRK1B (IC_{50} = 17 nM) and DYRK1A (IC_{50} = 88 nM) [39]. Its high potency ensured robust target engagement needed for structural interrogation, while its limited selectivity between the paralogs exemplifies the major challenge in the field. Nevertheless, AZ191 remains a practical tool compound, having been used to delineate DYRK signaling, including phosphorylation of cyclin D1a, substrate of both DYRK1A and DYRK1B [39].

In this work, we present the first crystal structure of human DYRK1B in complex with AZ191. To minimize the influence of inhibitor variability in our comparative analysis, we also determined the structure of DYRK1A in complex with the same inhibitor, AZ191. This allows us to map the precise interactions anchoring the inhibitor in the active site, providing a critical template for identifying subtle differences between DYRK1B and DYRK1A that can be exploited for the rational design of selective next-generation inhibitors.

2. Results

2.1. The pivotal role of autophosphorylation in maintaining DYRK1B stability

In the process of purifying the kinase domain of DYRK1B, it was observed that a substantial portion of the kinase aggregated in the insoluble fraction after cell lysis. This observation is particularly relevant considering the established importance of tyrosine phosphorylation within the Tyr-Xxx-Tyr motif for the enzyme's catalytic functionality and structural stability, as documented in prior studies [37,40,41]. Given this background, we hypothesized that the autophosphorylation of DYRK1B might be suboptimal when expressed in *Escherichia coli*. To investigate this, we specifically assessed the phosphorylation status of Tyr273. This was achieved through mass spectrometry analysis conducted on the whole cell lysate.

The Tyr273 was clearly visible during cell lysate analysis, mainly in the unphosphorylated form. Specifically, peptides: [253–277], [257–277], [157–280], and [270–280] (Uniprot ID Q9Y463) were identified based on their numerous MS/MS spectra (details in supplement: „identification report”). We detected Tyr273 phosphorylation in some of these peptides; however, the ratio between phosphopeptide and their unphosphorylated forms appeared to be low. To estimate the level of Tyr273 phosphorylation, we compared peak areas of the corresponding peptides in both forms. We focused on the ions at m/z = 730.3836^{4+} (unphosphorylated [253–277]) and at m/z = 750.3749^{4+} (phosphorylated [253–277]). The identities of both peptides were verified by their fragmentation spectra to confirm the sequences and phospho-residue (Figs. S1 and S2). The observation that the final, stable protein pool was completely phosphorylated at Tyr273 - in stark contrast to the initial 14 % phosphorylation in the lysate (Calculated area corresponding extracted ion chromatogram, Fig. S3) - supports the hypothesis that the unphosphorylated or partially phosphorylated forms of DYRK1B are prone to aggregation and are selectively lost during purification.

2.2. AZ191, a potent and selective DYRK1B inhibitor, enables paralog differentiation

The thermal-shift assay revealed that the catalytic domain of DYRK1A and DYRK1B has a markedly distinct thermal profile despite

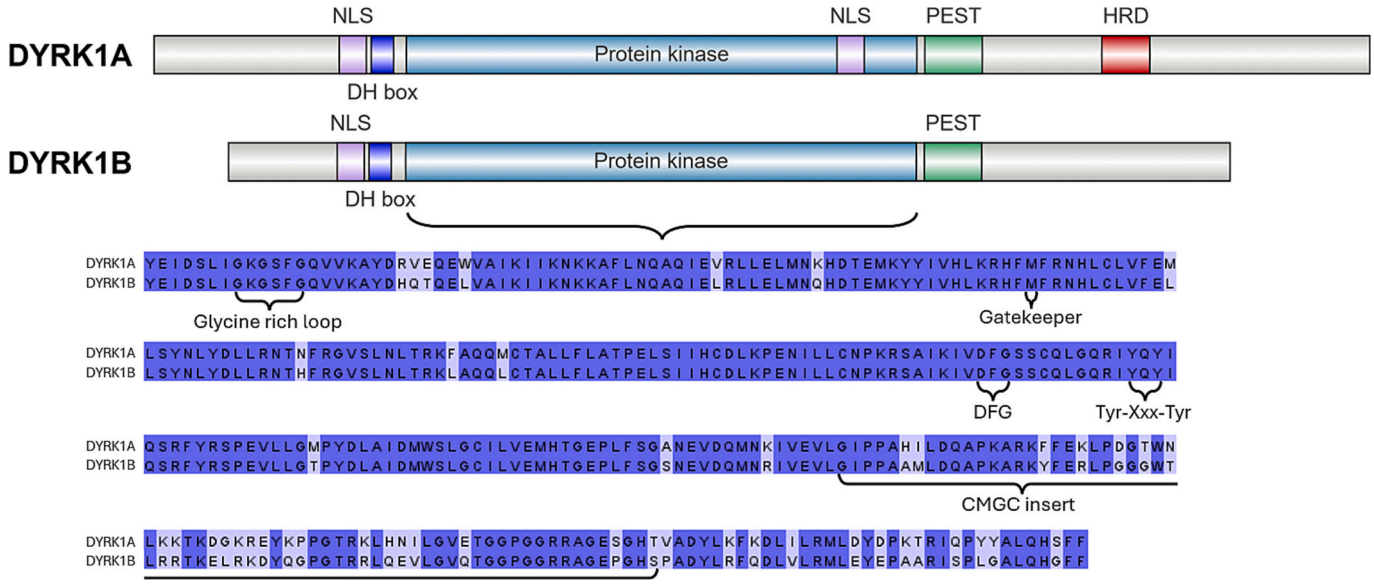

Fig. 1. Schematic arrangement of domains in human DYRK1A and DYRK1B.

the high sequence identity (over 85 %). The kinase domain of DYRK1A (124–490) was more stable with a melting point of 56 °C (T_m), while the thermal denaturation of the kinase domain of DYRK1B (78–442) was observed at 47 °C (T_m) (Fig. 2B and Table S1). This difference in melting temperatures aligns with previous observations and supports the distinct stability profiles of these two proteins [42]. Both DYRK1s' stability was improved, and their melting temperature was raised by binding of harmine or AZ191. Notably, AZ191 at 10 μM induced a remarkable 12 °C shift in T_m of DYRK1B, indicating a strong stabilizing effect. AZ191 had a less pronounced impact on DYRK1A, with only a 4 °C shift observed. On the other hand, Harmine exhibited a moderate stabilizing effect, causing a 1.5 °C and 2.5 °C increase in melting temperatures of DYRK1A and DYRK1B, respectively (Fig. 2B and Table S1). To provide a more comprehensive context for our findings regarding the significant stabilization of DYRK1B by the AZ191 inhibitor, we conducted a Cellular Thermal Shift Assay (CETSA). The thermal stability was assessed for the full-length DYRK1B expressed in HEK293 cells and treated with the inhibitor (10 μM) or DMSO. For DYRK1B and DYRK1B-AZ191, denaturation occurred gradually over a wide temperature interval. However, an increased thermal stability of the full-length DYRK1B was observed following treatment with the AZ191 inhibitor (Fig. S4). This provides evidence that AZ191 binds to and enhances the stability of both the isolated kinase domain and full-length DYRK1B.

The AZ191-induced thermal stabilization of DYRK1A and DYRK1B kinases prompted us to investigate the impact of the inhibitor on the kinase activity profile. We employed the ADP-Glo kinase activity assay to quantify the inhibitory potency of AZ191 (IC_{50}) against DYRK1A and DYRK1B. In the assay, purified kinase domains of DYRK1A or DYRK1B (5 ng/μl) were titrated with the inhibitor (5 nM – 5 μM) in the presence of ATP (100 μM) and a synthetic peptide substrate (400 μM). The ATP concentration was chosen based on the experimentally determined K_M for DYRK1A and DYRK1B of 118 μM and 105 μM, respectively. AZ191 strongly inhibited DYRK1B and DYRK1A, with IC_{50} in the nanomolar range (Fig. 2C and Table S1). Notably, the inhibitory effect was more pronounced for DYRK1B, with an IC_{50} of 66 nM, whereas for DYRK1A, the IC_{50} was 188 nM. These results are consistent with previously reported data, IC_{50}(DYRK1B) of 18 nM, IC_{50}(DYRK1A) of 199 nM and IC_{50}(DYRK1B) of 83 nM, IC_{50}(DYRK1A) of191 nM in radiometric assay and proximity assay, respectively [32]. For comparison, IC_{50} values were determined for harmine using the same assay conditions. Harmine inhibits DYRK1A and DYRK1B with IC_{50} of 97 and 115 nM, respectively.

The binding affinities of harmine and AZ191 to DYRK1A and DYRK1B were also evaluated by isothermal titration calorimetry (ITC) (Figs. 2D and S5, Table S1). AZ191 demonstrated a binding affinity of 54 nM to DYRK1A and a stronger binding affinity of 28 nM to DYRK1B, suggesting a slight preference in binding to DYRK1B over DYRK1A. The study also indicated that harmine exhibited a binding affinity of 94 nM to DYRK1A and 29 nM to DYRK1B. Beyond binding affinity, the thermodynamic profiles of the inhibitors provide significant insight into their mechanism of interaction and structural impact. The binding of harmine to both DYRK1A and DYRK1B is predominantly enthalpically driven ($\Delta H = -48.1$ and -59.2 kJ mol^{-1}, respectively) but is counteracted by a significant entropic penalty ($-T\Delta S = +7.9$ and $+16.2$ kJ mol^{-1}). This thermodynamic signature is consistent with the modest thermal stabilization observed *via* NanoDSF (ΔTm of +1.0 °C for DYRK1A and + 2.5 °C for DYRK1B). In stark contrast, AZ191 exhibits a more favorable thermodynamic profile. Its binding to DYRK1A is driven by both favorable enthalpy and entropy ($\Delta H = -23.7$ kJ mol^{-1}; $-T\Delta S = -17.8$ kJ mol^{-1}), while its interaction with DYRK1B is strongly enthalpy-driven with only a minor entropic penalty. This explains the markedly greater thermal stabilization conferred by AZ191, which produced a substantial ΔTm of +4.0 °C for DYRK1A and + 12.0 °C for DYRK1B. These data suggest that while both inhibitors achieve nanomolar affinity, AZ191 forms a more thermodynamically stable complex, likely through interactions that do not require the same degree of conformational ordering or restriction as harmine. This differential binding may reflect potential selectivity, which could be further explored for therapeutic implications, especially in designing selective inhibitors for DYRK1B.

The CETSA results confirmed the cellular interaction between DYRK1B and AZ191, as evidenced by the thermal stabilization of the protein. However, these results did not directly demonstrate the inhibition of DYRK1B kinase activity. To address this, we decided to investigate the effect of the AZ-191 inhibitor on the DYRK1B-controlled calcineurin/NFAT (Nuclear Factor of Activated T Cells) pathway. This signaling pathway is crucial in various biological processes, including immune response and neuronal development. DYRK1B-mediated phosphorylation of NFAT prevents its translocation from the cytoplasm to the nucleus, thereby inhibiting gene transcription [43]. The cellular localization of NFAT, which depends on its phosphorylation status, is a valuable indicator of DYRK1B kinase activity.

We utilized a cellular assay to track the translocation of EGFP–NFATc1 between the cytoplasm and the nucleus. In cells co-expressing mCherry-DYRK1B and EGFP–NFATc1, we observed predominant

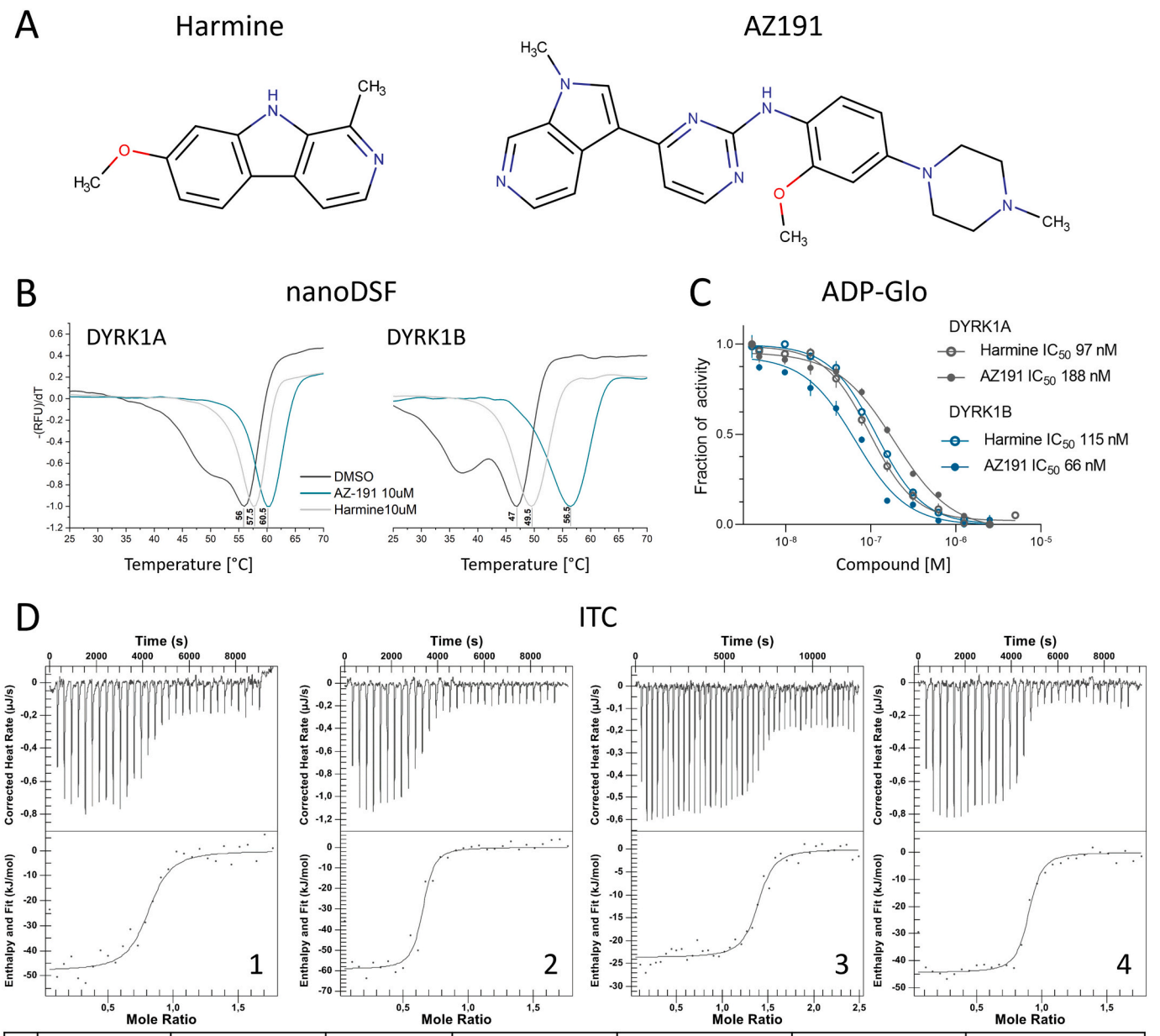

	Protein	Compound	K_d [nM]	N	ΔH [kJ mol^{-1}]	-TΔS [kJ mol^{-1}]	ΔG [kJ mol^{-1}]
1	DYRK1A	harmine	94.02	0.796 ± 0.033	-48.05 ± 3.241	7.936	-40.11
2	DYRK1B	harmine	29.38	0.630 ± 0.018	-59.15 ± 2.926	16.150	-42.99
3	DYRK1A	AZ191	54.63	1.370 ± 0.028	-23.67 ± 0.819	-17.780	-41.45
4	DYRK1B	AZ191	28.08	0.877 ± 0.014	-44.47 ± 1.341	1.362	-43.11

Fig. 2. Biochemical analysis of DYRK1's interactions with harmine and AZ191. (A) Structure of harmine and AZ191. (B) Thermal denaturation curves (first derivative) of DYRK1A (left panel) and DYRK1B (right panel) kinase domains after treatment with harmine, AZ191, or DMSO as determined in the Sypro Orange dye monitored thermal shift assay. (C) Inhibitory activity of AZ191 and harmine against DYRK1A and DYRK1B determined in ADP-Glo kinase activity assay and (D) ITC, representative trace from experiments performed in triplicate.

cytoplasmic localization of EGFP–NFATc1 (Fig. 3A). This localization persisted even upon stimulation with ionomycin, a known activator of calcineurin, indicating that mCherry-DYRK1B effectively restrained the nuclear translocation of EGFP-NFATc1 (Fig. 3B). However, upon treatment with 10 μM of AZ191, a marked translocation of EGFP–NFATc1 to the nucleus was observed despite the presence of mCherry-DYRK1B (Fig. 3C). This demonstrates that a concentration of 10 μM of AZ191 inhibits DYRK1B activity and thereby restores the functionality of the calcineurin/NFAT pathway in our cellular model.

2.3. Structural analysis of DYRK1 kinases with AZ191

2.3.1. Crystal structure of DYRK1B in complex with AZ191

Alexandrov et al. [44] reported a pipeline for optimizing selective inhibitors for DYRK1B. However, the key challenge in this and other structure-based design approaches was the lack of an experimental structure for DYRK1B. Addressing this gap, we successfully expressed, purified, and crystallized the kinase domain of DYRK1B (residues 78 to 442; Uniprot ID Q9Y463) in complex with the inhibitor AZ191 (PDB ID

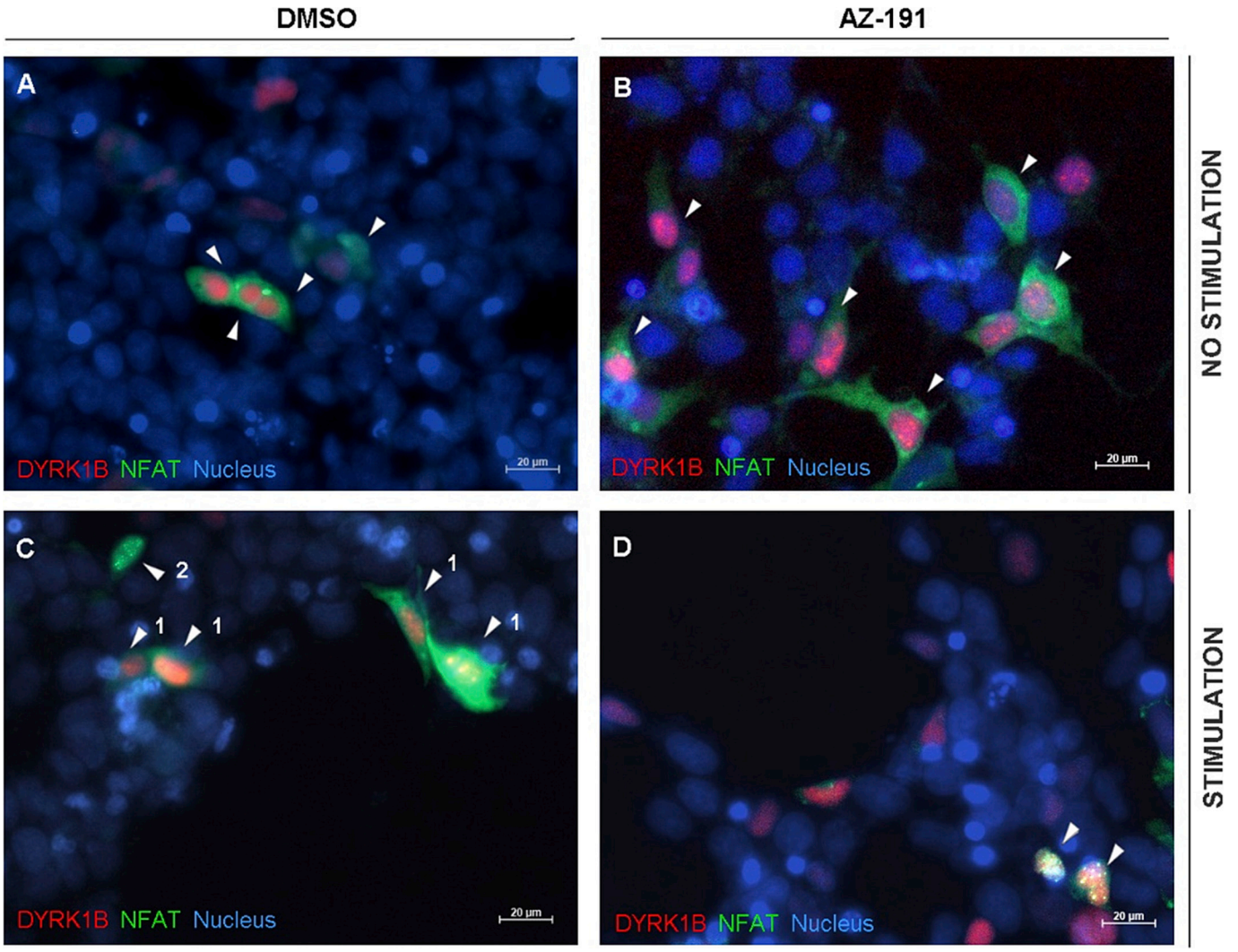

Fig. 3. AZ191 treatment restores NFAT signalling by blocking DYRK1B kinase activity. The EGFP–NFATc1 (green) and mCherry-DYRK1B (red) were co-expressed in HEK293T cells. Cells pre-treated for 3 h with AZ191 (10 μM) (B,D) or DMSO (A,C) and stimulated for 1 h with ionomycin (IM; 6 μM) (C,D) or left untreated (A, B). The representative fluorescent images are shown with a scale bar 20 μm.

8C2Z). The kinase crystallized in the $C222_1$ space group, featuring a single molecule per asymmetric unit. The structure, resolved at a 1.91 Å resolution, clearly delineates most of the molecule, except for portions of the CMGC kinase-specific insert (residues 382–394). Furthermore, residues 118–124 in the glycine-rich loop, residues 248–253, residues 266–273 within the activation loop and the regions encompassing additional parts of the CMGC insert (residues 357–369, 378–381 and 395–400) exhibit higher temperature factors compared to the rest of the molecule. This observation suggests that these areas possess structural flexibility, which could be crucial for understanding the kinase's functional dynamics and designing more effective inhibitors.

The overall structure of DYRK1B resembles that of protein kinases of the CMGC group, with a bilobal fold and the active site located in a cleft formed between these lobes. The structure is seen in the active DFG-in conformation. The smaller N-terminal lobe mostly comprises β-sheets and contributes the catalytic lysine (Lys140). The larger C-terminal lobe is composed primarily of α-helices and contributes the activating tyrosine residue within the Tyr271-Xxx-Tyr273 motif. A clearly defined electron density indicates Tyr273 phosphorylation (Fig. S7). Since the kinase was expressed in bacteria, where posttranslational modifications are relatively rare compared to eucaryotes, it is likely that the modification results from autophosphorylation. This is in good agreement with previous findings suggesting that DYRK1B undergoes autophosphorylation [40]. Overall, the crystal structure of the DYRK1B kinase domain determined in this study overlays well with DYRK2 (PDB ID 4AZF) and DYRK3 (PDB ID 5Y86). The RMSDs are 0.85 Å for 74.6 % of C_α atoms and 0.77 Å for 73.1 % of C_α atoms for DYRK2 and DYRK3, demonstrating the high structural similarity.

AZ191 exemplifies an ATP mimetic kinase inhibitor and, accordingly, is located at the putative ATP binding site of DYRK1B (Fig. 4A and B). The pyrimidine ring contributes a canonical interaction with the backbone amine of Leu193 within the hinge region. The methylpyrrolopyridine group penetrates deep into the pocket towards the catalytic Lys140. This moiety is stabilized by a direct hydrogen bond with the side chain aminium of Lys140, π-stacking interactions with the sidechains of the gatekeeper residues Phe190 and Phe122, and hydrophobic interactions contributed primarily by the sidechains of Val125 and Val258. The methylpiperazine moiety of AZ191, commonly found in several kinase inhibitors, generally protrudes out of the pocket into the solvent, which is also observed in our structure. However, what is characteristic of AZ191, however, is that the methylpiperazine contributes to affinity by forming a hydrogen bond with the sidechain carboxyl of Asp199. Additionally, this methylpiperazine contributes a water-mediated hydrogen bond with the main chain of Ile117. The methoxyphenyl linker contributes a π-lone pair interaction with the backbone carbonyl of Ser194, a hydrogen bond with Leu193, and

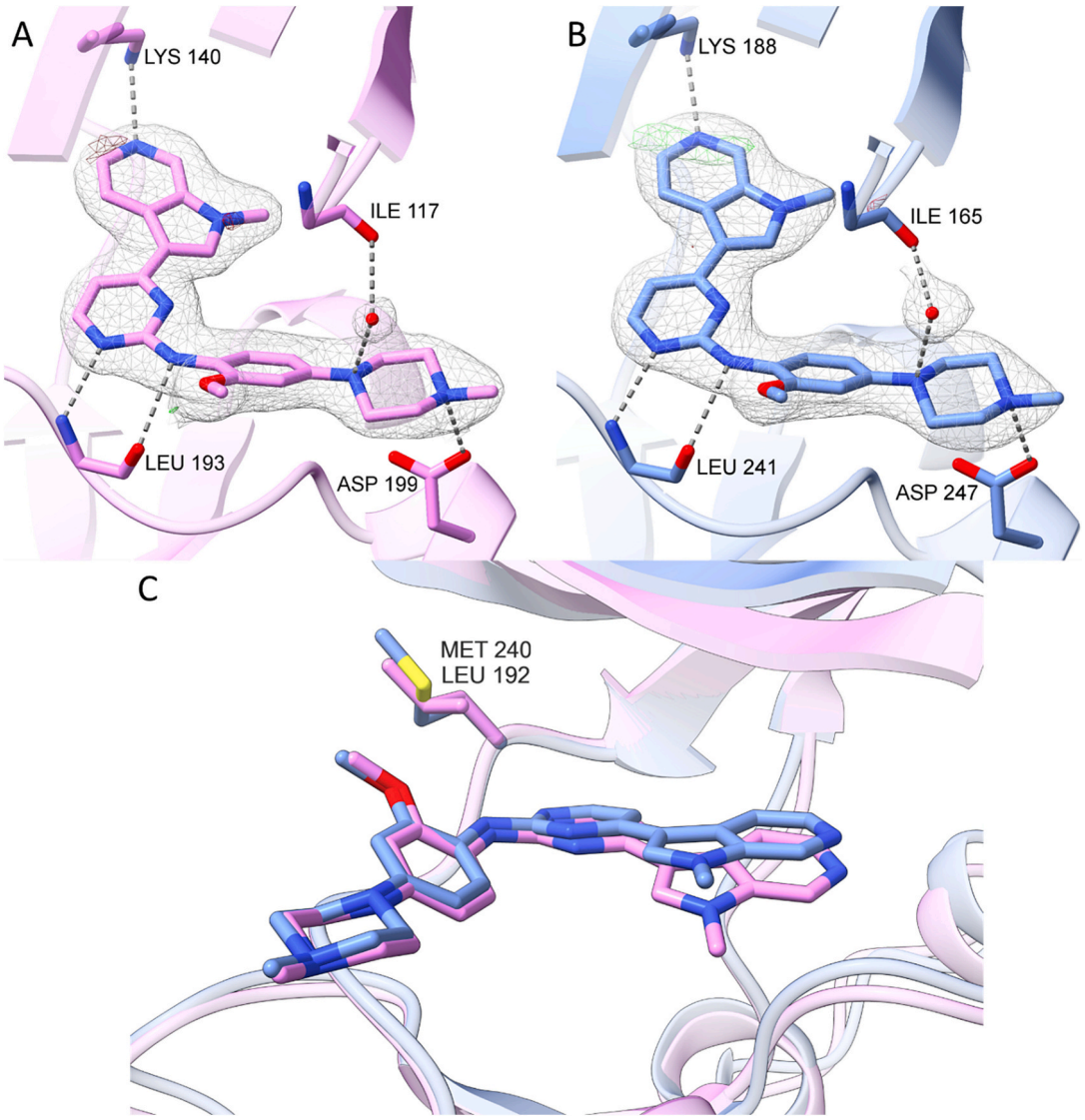

Fig. 4. Crystal structures of DYRK1B (pink) and DYRK1A (blue) in complex with AZ191. (A) the binding mode of AZ191 in the ATP-binding pocket of DYRK1B (PDB ID 8C2Z), (B) binding mode of AZ191 in the ATP-binding pocket of DYRK1A (PDB ID 8C3G), (C) superimposition of DYRK1B and DYRK1A ATP-binding pockets with indicated single amino acid difference between their active sites. Hydrogen bonds are shown as dashed lines (dark grey) and the electron density is shown as a mesh, 2Fo-fc: +1.0σ (light grey); Fo-Fc omit map: +3.0σ (green); Fo-Fc omit map: -3.0σ (red).

hydrophobic interactions with the sidechain of Ile117. The methoxy substituent stabilizes the rotation of the moiety at the binding site.

Phosphorylation of Tyr273 provides an anchor point for a network of hydrogen bonds stabilizing the position of the Tyr273 sidechain at the surface of the kinase. These include salt bridges with the guanidine moieties contributed by Arg277 and Arg280. A water-mediated hydrogen bond with the sidechain of Ser276 further stabilizes the sidechain of Tyr273 and, thereby, the orientation of the Leu266-Ser276 linker. This region constitutes the peptide substrate binding site and is unstructured in related unphosphorylated kinases. Thus, phosphorylation regulates the activity by stabilizing the substrate binding cleft, as previously described for other kinases of the CMGC group.

2.3.2. Crystal structure of DYRK1A in complex with AZ191

DYRK1B and DYRK1A kinases share a sequence identity of 85 % among the catalytic domain residues. The identity is even higher for residues composing the active site. At such high evolutionary relatedness, the design of selective inhibitors is highly challenging, and success relies on subtle differences at the active site. A total of 83 crystal structures of DYRK1A in complex with inhibitors have been solved and reported. Collectively, this data allows us to compare our DYRK1B structure in search of specificity anchor points, but minor differences are best indicated when using structures with identical inhibitors. Consequently, we determined the structure of the DYRK1A kinase domain (residues 126–489, Uniprot ID Q13627) in complex with AZ191 (PDB ID 8C3G).

The DYRK1A in complex with AZ191 crystalized in the $P2_12_12_1$ space group, and the asymmetric unit comprised 4 molecules. The crystals diffracted to 2.08 Å resolution. A well-defined electron density documents phosphorylation at the Tyr321 residue (Fig. S7 B-E). Accordingly, the structure reflects that of a catalytically competent enzyme. Each kinase molecule in the asymmetric unit contains a clearly interpretable electron density describing the inhibitor (Fig. S7 B-E). The protein molecules in the asymmetric unit are virtually identical, and the inhibitor dispositions at the active site of each molecule in the asymmetric unit do not differ. Thus, only model A is considered in further analysis.

The interactions guiding the inhibitor affinity are virtually identical to those observed in DYRK1B (Fig. 4A and C). Hydrogen bonds contributed by the sidechains of the catalytic Lys188, Asp247, and the

mainchain of Leu241 in the hinge region (equivalent to Lys140, Asp199, and Leu193 of DYRK1B, respectively) anchor AZ191 to the active site of DYRK1A. Further, the methylpiperazine moiety contributes a water-mediated hydrogen bond with the main chain of Ile165 (an equivalent interaction is found with Ile117 in DYRK1B). However, the said water is found only in molecules A and C. Further, the inhibitor is stabilized by major hydrophobic interactions contributed by Ile165, Phe170, Val173, Phe238, Leu294, and Val306 (equivalent to Ile117, Phe122, Val125, Phe190, Leu246 and Val258 of DYRK1B, respectively).

When comparing the AZ191 inhibitor in the co-crystal structure with DYRK1B to that with DYRK1A, different orientations of the methylpyrrolopyridine moiety are observed (Fig. 5). In the structure of DYRK1B, the aromatic group is positioned closer to the C-lobe region. The difference, however, is not expected to be related to the fine details distinguishing the kinase active sites but rather reflects the different crystallization conditions, which, in the case of DYRK1B, further contained Mn^{2+} ions. In the DYRK1B structure, the manganese ion coordinates the side chains of Asp239 and Asp259, reorienting them away from the ATP binding pocket. This affords additional space for methylpyrrolopyridine reorientation when compared to DYRK1A. In the structure with DYRK1A, the absence of manganese ion allows the side chain of Asp307 (corresponding to the Asp259 in DYRK1B) to displace the methylpyrrolopyridine group of AZ191 towards the N-lobe. Apart from the influence of the ion, the binding modes of AZ191 at the active site of DYRK1B and DYRK1A are virtually identical, reflecting the comparable affinity of the inhibitor to both kinases (Fig. 2C and Table S1).

Despite the overall identity of the binding sites and inhibitor stabilizing interactions, the direct overlay of DYRK1B and DYRK1A crystal structures in complex with AZ191 points to a notable difference in the overall structures of the kinases. The active site of DYRK1B is narrower than that of DYRK1A, which is related to the closing of the N- and C-terminal lobes around the hinge region. The N-lobes of DYRK1B (residues 88–190) and DYRK1A (124–238) show a high degree of structural similarity, with RMSD of 0.34 Å for 75.7 % of C_α atoms (Fig. S6A). The C-lobes (residues 197–434 and 245–490 for DYRK1B and DYRK1A, respectively) also display a similar pattern, with RMSD of 0.39 Å for 72.3 % of C_α atoms (Fig. S6B). However, when comparing the overall structures of the kinase domains, the RMSD is 0.89 Å for 80.5 % of Cα atoms. The increase in RMSD suggests that the N- and C-lobes are oriented differently relative to each other in the two kinases. To determine whether the differences in the relative orientation of the N- and C-lobes are characteristic of DYRK1B, we compared its structure against all available crystal structures of DYRK1A. From this structural evaluation, we concluded that this scissor-like relative relocation of the lobes around the hinge is characteristic of DYRK1A, and our structure with AZ191 represents one of the multiple relative orientations of the lobes. Other structures of DYRK1A present this reorientation of the lobes

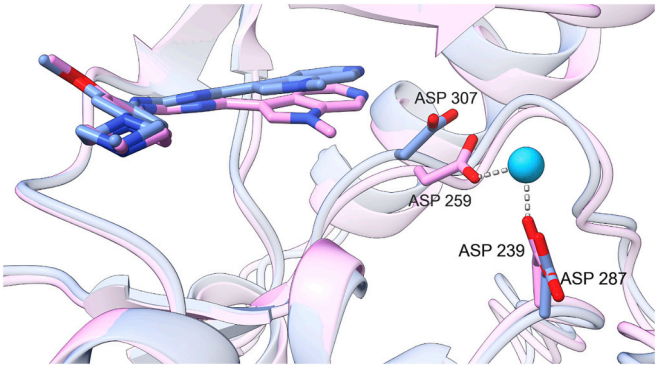

Fig. 5. Superimposition of DYRK1B (pink) and DYRK1A (blue) in complex with AZ191 (PDB ID 8C2Z and 8C3G, respectively) with indicated Mn^{2+} ion bound to DYRK1B.

almost identical to our structure of DYRK1B (*e.g.*, PDB ID 2VX3; RMSD of 0.49 Å for 75.4 % of C_α atoms). The apparent relative motions of the N- and C- lobes are partly related to crystal packing. The structure of DYRK1A closest to our present one in complex with AZ191 was determined in the same space group (*e.g.*, PDB ID 7FHT; RMSD of 0.30 Å for 89.8 % of C_α atoms). On the other hand, the most distal structures with respect to the currently presented structure of DYRK1A with AZ191 were obtained in different space groups. Overlaying our crystal structure of DYRK1B with the most closely related structure of DYRK1A shows overall negligible differences.

Apart from the differences induced by crystal packing and crystallization conditions, the ATP binding pockets of DYRK1B and DYRK1A are practically indistinguishable, except for a single residue at the hinge region (Fig. 4C). In the structure of DYRK1B, the sidechain of Leu192 is close to the methoxy group in the inhibitor, though it does not contribute to significant interactions. The equivalent residue in DYRK1A, Met240, has a slightly longer sidechain, which comes closer to the inhibitor. Convenient exploration and optimization of these interactions by modifications of substituents at the phenyl ring of AZ191 should allow for tackling the specificity of this class of inhibitors. Other scaffolds could also explore this pocket to achieve selectivity.

2.4. Computational insights into inhibitor binding in DYRK1 kinases

2.4.1. Quantum mechanical binding analysis

Despite the overall structural similarity and an almost exact identity in the binding pocket, DYRK1A and DYRK1B show different binding affinities ($\Delta G = RT \log[K_d]$) and selectivity towards inhibitors. The binding affinities towards AZ191 differ by a factor of two ($\Delta\Delta G \sim 0.41$ kcal/mol). Differences in other thermodynamic data are more pronounced, like binding enthalpies, indicating subtle differences between the two kinases warrant further exploration. We employed our Energy Decomposition and Deconvolutional Analysis algorithm (EDDA) to better understand the underlying mechanisms behind such fine selectivity [45]. EDDA is a quantum mechanicsbased algorithm that partitions interaction energies into different contributions. These components include electrostatics, polarization, dispersion (lipophilicity), repulsion (shape complementarity), solvation, and charge transfer. The EDDA algorithm allows determining the nature of protein-ligand interactions, allowing the quantification of the main forces that lead to binding. For a detailed algorithm description, please refer to the Supporting Information (SI) section 2 and the original paper [45]. Fig. 6 collects the electrostatics, dispersion (lipophilicity), repulsion, and total interaction maps for the inhibitor AZ191 in DYRK1A and DYRK1B. Fig. 6 also contains a column plot of decomposed energies. Additional maps and the respective calculated values are given in supplemental information (Figs. S8 - S10 and Table S3). To better place our results in the context of selective DYRK inhibitor design, we added an analysis of AZ191 docked to DYRK2 to the supplement (Figs. S15 - S22 and Table S9).

The initial observation when analysing the maps for AZ191 in each kinase is that the interaction landscape is virtually indistinguishable between the two DYRKs analysed (Fig. 6 A-D). This reflects the sequence homology around the ATP binding pocket. The ligand's main foci of interactions are N5, which binds to the catalytic lysine; N15 and N16 atoms, which interact with the hinge region; and the external nitrogen from the piperazine moiety. Despite the similarity, the total interaction maps (Fig. 6D) reveal stronger binding to the hinge of DYRK1B than to DYRK1A. The total interaction energies, comparable to enthalpies of binding, differ by 5.4 kcal/mol (in favour of DYRK1B), which correlates with the 5.0 kcal/mol measured by ITC. This establishes a strong agreement between our experimental and computational data. The electrostatics maps (Fig. 6A) show more polar interactions in the case of DYRK1A, which, when combined with the repulsion and charge transfer maps, indicate a lower covalent character for the hydrogen bonds in this kinase. It is particularly interesting in the case of the linker N16, where

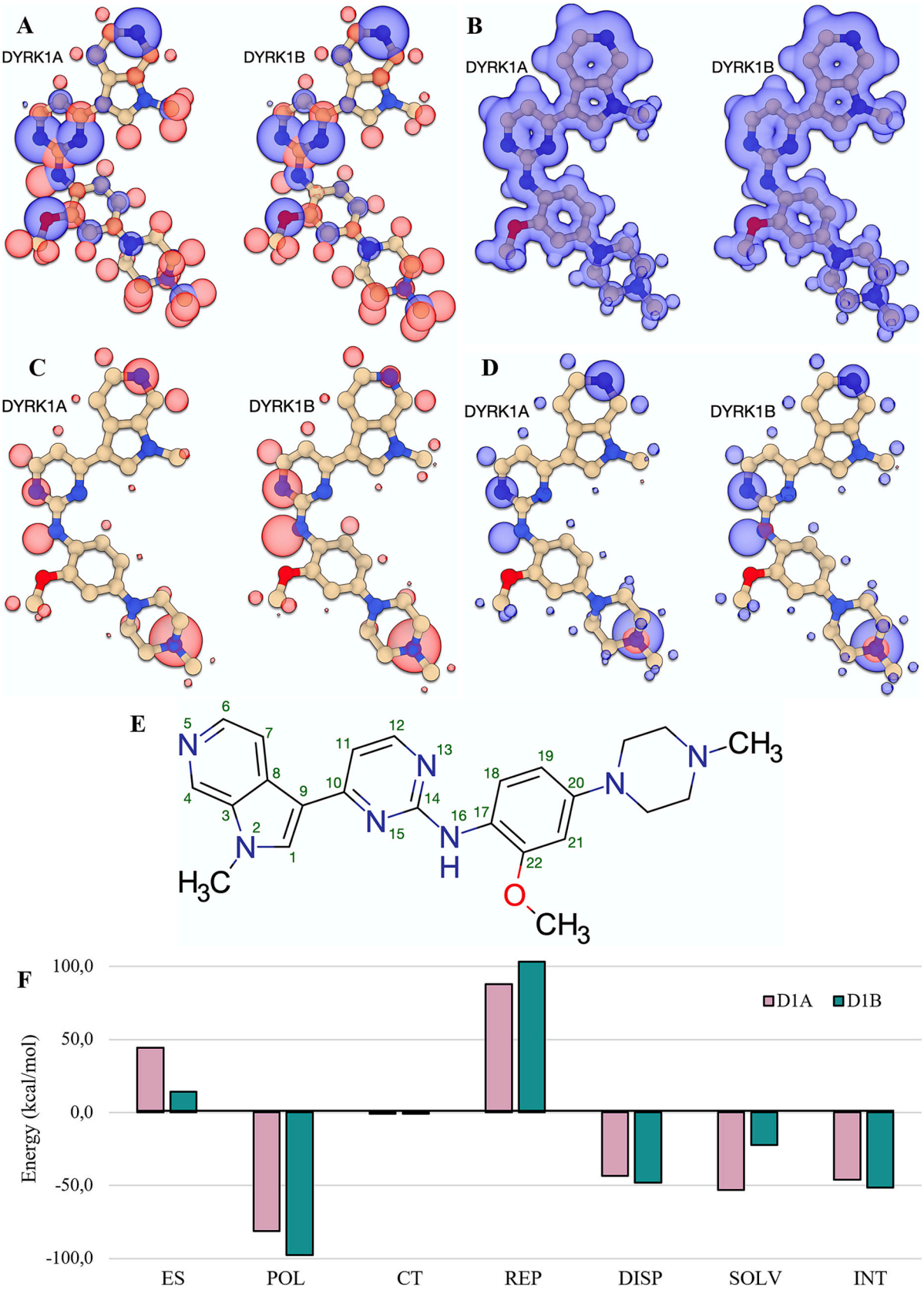

Fig. 6. The decomposition analysis of the binding energy of AZ191 in DYRK1A and DYRK1B. (A) The electrostatics (ES), (B) dispersion (DISP), (C) repulsion (REP), and (D) total interaction imaps for AZ191 in the kinases. (E) The structure of the ligand and the atomic numbering used in the discussion. (F) Decomposed energies.

the differences in maps are pronounced. Interestingly, the distance between N15 and N16 to the hinge binding atoms is shorter in DYRK1B by almost 0.2 Å for each bond. Repulsion maps (Fig. 6C), which measure the overlap of electronic densities between ligand and protein, indicate stronger contacts with DYRK1B. This evidences that the higher covalent character in the hydrogen bonds between AZ191 and the kinase's hinge is primarily an effect of atomic proximity and is less dependent on the protein's charge distribution.

The interaction of N5 with the catalytic lysine is weaker in the case of DYRK1B. While not apparent from the electrostatics viewpoint, this difference is evident in the repulsion and total interaction maps. Again, the effect seems to be primarily distance-related (local), as in DYRK1A, this hydrogen bond is shorter by almost 0.4 Å. Lastly, the interactions between the piperazine group and the proteins are identical.

To understand whether the different interactions with the hinge region and the catalytic lysine are significant from the binding perspective or whether these result from crystal artefacts (*e.g.*, lacking the dynamics of the protein-ligand complex), we analysed the total repulsion energy for each complex. Overall, repulsion is larger in DYRK1B by 15 kcal/mol (Fig. 6F), indicating a stronger overlap of protein and ligand electronic densities. This difference can also be observed in the respective maps (Fig. 6C), which show more intense contacts between DYRK1B and the ligand. The only exception is N5, the atom involved in interacting with the catalytic lysine, where the interaction is noticeably stronger in DYRK1A. Overall, the calculations indicate that AZ191 captures DYRK1B more effectively by the hinge region, whereas in DYRK1A, the interactions with the hinge and the catalytic lysine are more balanced. Indirectly, this hints that the accessibility of the catalytic lysine of DYRK1B is lower and could be a useful feature for achieving selectivity.

2.4.2. A role for the CMGC insert

The CMGC insert is one of the most variable regions between DYRK1A and DYRK1B, with a sequence identity of 66 % (compared to the 85 % for the kinase domains). However, only one of these differences alters the amino acid's charge state. Since the CMGC region was excluded from previous calculations, we reran our EDDA analysis using the full, experimentally determined kinase constructs.

Fig. 7A compares the DYRK1A-DYRK1B EDDAs for two system reconstructions: the large kinase domains analysed in the previous section *versus* the full kinase domains obtained from X-ray crystallography experiments. The total relative binding energies remain similar, further reinforcing the robustness and convergence of the previously calculated values. However, the absolute binding energy values vary due to changes in the protein's total charge. Notably, in the full constructs, the protein component of the complex becomes more positively charged, leading to an overall weakening of the total interaction. This effect is furthermore strongly reflected in the relative electrostatic and solvation contributions, as shown in Fig. 7A. Specifically, the electrostatic repulsion between DYRK1A and AZ191 increases when considering the full kinase domain, including the CMGC insert. In contrast, electrostatic interactions between DYRK1B and AZ191 become predominantly attractive, indicating an inversion of the electrostatic interaction pattern in the case of DYRK1B. Interestingly, the solvation contributions to binding in DYRK1A remain unchanged when using the full protein system in the calculations. On the other hand, for DYRK1B, the solvation terms become repulsive. These findings align with our previous observations regarding electrostatics. While differences exist in other binding forces (CT-POL, REP, DISP), they are less significant than the effects of electrostatic interactions and solvation.

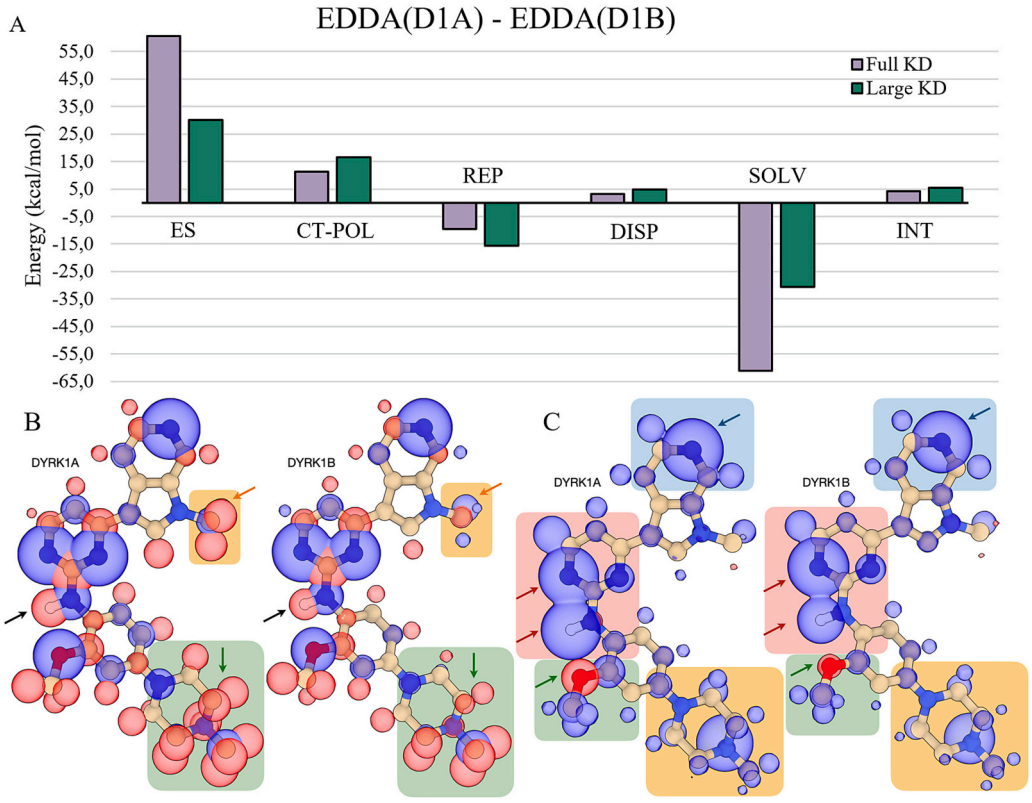

Fig. 7. The binding energy decomposition analysis of AZ191 in the full kinase domains of DYRK1A and DYRK1B, compared against the large pocket previously analysed in Figure 6. We coupled the POL and CT interactions because the underlying algorithm needed to split these terms has poor convergence properties with system size. A) The differential EDDA plot, where each interaction contribution in the DYRK1B-AZ191 complex is subtracted from the respective contribution in the DYRK1A-AZ191 EDDA. KD in the legend stands for Kinase Domain. B) The ES maps for AZ191 in each of the DYRK1 kinases using the full kinase domains. The main regions where the maps differ are highlighted with yellow and green backgrounds. C) The total interaction maps (INT) for AZ191 in each of the DYRK1 kinases, using the full kinase domain. The main regions where the maps differ are highlighted with yellow, green, blue, and red backgrounds.

At first glance, the EDDA interaction maps calculated with the full kinase domains show no significant changes in interaction patterns (Fig. 7B and C), with the overall map composition largely conserved compared to our previous calculations (Fig. 6A and D). This shows that the first amino acid shells are the primary drivers of protein-ligand interactions and that expanding from the large kinase domains used in the previous section to the full kinase domains in the new calculations only incorporates long-range interactions. However, we do observe differences in the relative contributions of ligand functional groups involved in non-specific and non-directional interactions. These may influence kinase selectivity based on ligand electronic properties. For example, the electrostatic interaction pattern differs around AZ191's methyl-pyrrolopyridine moiety (yellow highlighted region in Fig. 7B). The increased repulsive interactions in the DYRK1A complex suggest that modifying the electronic properties of this exposed functional group could provide valuable structure-activity relationship (SAR) insights. Similarly, our calculations indicate a comparable effect for AZ191's piperazine group (green highlighted region in Fig. 7B). Although this piperazine moiety is in proximity to an Asp residue (Asp247 in DYRK1A, Asp199 in DYRK1B), it does not fully disrupt the interaction between this Asp's carboxylate and a nearby Arg residue (Arg250 in DYRK1A, Arg202 in DYRK1B). Similar observations are made when analysing the total interaction maps (INT) around this group (Fig. 7C). The INT maps highlight additional ligand modifications that could be of interest for SAR exploration. AZ191's interactions with DYRK1A's catalytic lysine are strengthened compared to those with DYRK1B (blue highlighted region). Differences are also observed in the interaction patterns around the hinge region of each kinase (red highlighted region), suggesting that variations in the hydrogen-bonding properties of hinge-binding groups may yield valuable SAR insights. This was also reflected at the ES-interaction level, as seen by the black arrows in Fig. 7B. A closer look at the maps indicates that, energetically, the interaction with the hinge has a stronger bidentate character for DYRK1A. Potentially, designing mono-dentate hinge binders will have less impact for DYRK1B inhibition than it does for DYRK1A. Similar observations were already noted in the previous section's analysis. A comparable trend is seen for the methoxy substituent on the aromatic ring linking the hinge-binding motif to the solvent-exposed piperazine. While our analysis is based on only two structures, limiting its reliability, we believe that further exploration of the interaction imbalance at the kinase hinge and the accessibility of the catalytic lysine could guide the development of the first DYRK1-selective ligands.

2.4.3. The interactions of DYRK1A and DYRK1B with harmine

Harmine, a small β-carboline alkaloid, is a potent DYRK1A inhibitor, exhibiting a lower potency against DYRK1B [32]. To better understand the electronic basis of this selectivity and how harmine inhibits kinases, we investigated the interaction of harmine with both DYRK1 kinases and compared them against the thermodynamic data we discussed above.

Given that we obtained high-resolution crystal structures of DYRK1A and DYRK1B bound to a common inhibitor, our structures served as the natural template choice for docking harmine. However, conventional docking approaches failed to yield meaningful results, likely due to the size and chemical topology differences between AZ191 and harmine. To overcome these limitations and to generate suitable protein-ligand structures, we used the CHAI-1 model [46] to construct plausible harmine binding poses in both kinases. The resulting models are highly consistent with one another (Fig. 8A) and closely match the experimentally determined crystal structure of harmine bound to DYRK1A (Fig. S23) [47]. These models provide a reliable foundation for further analysis using EDDA calculations (Fig. 8B).

Our results indicate that harmine binds more favorably to DYRK1A than to DYRK1B, with an estimated free energy difference of −3.46 kcal/mol. This is in good agreement with the experimental value we reported above for the relative binding enthalpy of −2.65 kcal/mol ($\Delta\Delta H = \langle\!\langle \Delta H \rangle\!\rangle\_DYRK1A - \langle\!\langle \Delta H \rangle\!\rangle\_DYRK1B$). The energy breakdown reveals that DYRK1A offers stronger electrostatic (ES) and slightly more favorable dispersion (DISP) interactions, despite showing lower electronic density overlap (REP). This suggests a more efficient chemical complementarity in the DYRK1A binding site.

Consistent with prior analyses of DYRK1-ligand complexes, the EDDA interaction maps for harmine in both kinases show broadly similar patterns. The electrostatic contributions are nearly indistinguishable (Fig. 8C), although subtle differences can be noticed. In the complex with DYRK1B, the interactions involving harmine's methoxy group (targeting the hinge region) and the pyridine ring (interacting with the catalytic lysine) appear more balanced. In contrast, harmine bound to DYRK1A shows slightly stronger engagement at the hinge, while in DYRK1B it exhibits greater steric repulsion at the pyrrole hydrogen. This contrasts with the results obtained for AZ191 in the DYRK1 kinases, indicating, expectedly, that the strength of inhibitor-hinge interactions is a major predictor of binding efficacy.

The repulsion maps highlight key contact points, particularly at the hinge region (Fig. 8D). Notably, in the DYRK1B complex, harmine experiences an additional repulsive interaction involving a hydrogen atom ortho to the methoxy substituent. Furthermore, protein-ligand contact points in DYRK1B are more dispersed across the ligand, as indicated by the red spheres around peripheral hydrogen atoms. This suggests that the DYRK1B binding pocket is more constricted than that of DYRK1A, at least according to the CHAI-1 predictions. We stress that the CHAI-1 model could not have been trained with any DYRK1B-specific data. Further, the ligand's ability to engage with the catalytic lysine differs notably, followed by variations in the magnitude of the repulsion contributions on the pyridine's nitrogen atom. Again, this correlates with the expected behaviour of type I kinase inhibitors like harmine.

We also analysed the total interaction maps (Fig. 8E). DYRK1A exhibits stronger repulsion at the indole nitrogen, while the remaining interaction patterns are largely unaffected. Given that all maps are normalised to the strongest interaction within each complex, these results indicate that the harmine–DYRK1A interaction is overall stronger, driven by enhanced interactions with the kinase's hinge and catalytic lysine.

Additional EDDA maps are provided in the Supplementary Information (Figs. S23 - S26 and Table S10).

2.4.4. The dynamics of DYRK1A and DYRK1B

To better understand the behaviour of DYRK1A and DYRK1B, apo and inhibitor complexes, a series of molecular dynamics (MD) simulations were conducted. MD and EDDA results on the MD traces are presented in Fig. 9 (see supplemental Tables S4-S7 for additional data).

The most direct observation from the apoprotein simulations is the larger flexibility of DYRK1A, as seen in the RMSD fluctuations of the dynamical traces (Fig. 9A). On average, the N- and C-lobes are more distal in DYRK1A, with wider amplitude movements (Fig. 9B). This is, however, a simulation artefact due to the extended time required for DYRK1A to relax from the initial structure with the ligand's imprint. After about 250 ns, DYRK1A closes the pocket, remaining in this state until the end of the simulation. This we identify as the resting state of the kinase, which is identical for both paralogs (Fig. S12).

Fig. 9C shows the time-averaged EDDA on both protein-ligand complexes. Interestingly, all interactions decrease in magnitude compared to crystal structure calculations. Most contradictory, the average shape complementarity becomes larger in DYRK1A. The average binding energy also favours DYRK1A, which contradicts experimental data. Though DYRK1B shows larger variations in binding energy, the EDDA binding energy as a function of time tendentially decreases for DYRK1A and increases for DYRK1B. These trends and the simulation snapshots indicate the inability of AZ191 to reach DYRK1B's catalytic lysine. This is reflected in the distances between the ligand's N5 and the NZ of the catalytic lysine (Fig. S13): on average, 3.17 Å for DYRK1A and 3.51 Å for DYRK1B, differ significantly from the experimental values of 2.92 and 2.97 Å, respectively. Though this imbalance

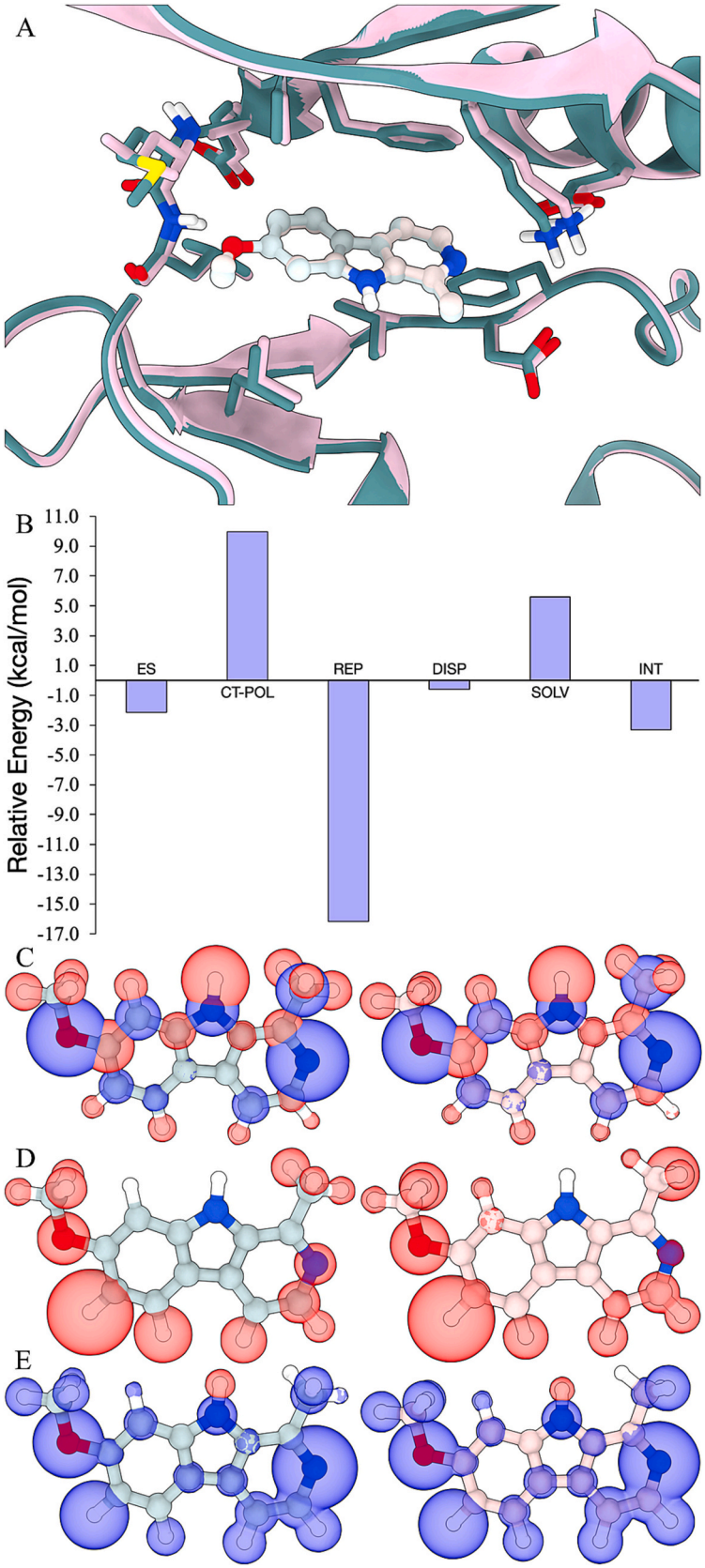

Fig. 8. Energy decomposition analysis of harmine in the DYRK1A and DYRK1B kinases. In this figure, the teal tonalities are reserved for DYRK1A and harmine bound to DYRK1A, whereas pink tones are used for DYRK1B and harmine bound to DYRK1B. A) The overlay of the CHAI-1-generated harmine-DYRK1A and harmine-DYRK1B models, showing an almost perfect overlay. B) Relative EDDA energetics, with the harmine-DYRK1B complex used as reference. A negative energy value indicates that the respective interaction type is stronger for DYRK1A. C) Electrostatic maps for harmine in each DYRK1 enzyme. D) Repulsion maps for harmine in each DYRK1 enzyme. E) Total interaction maps for harmine in each DYRK1 enzyme.

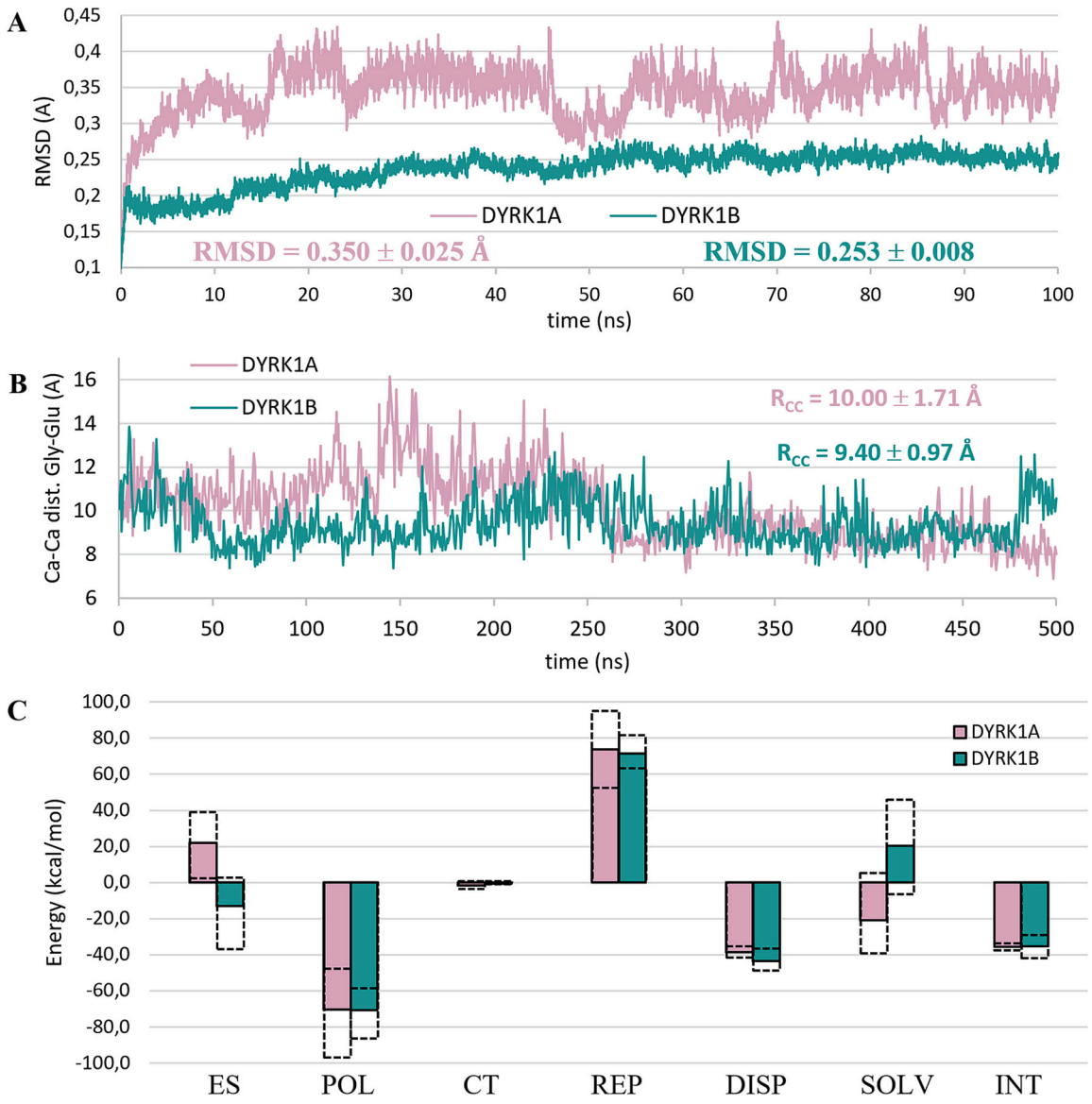

Fig. 9. The dynamics of the apo and AZ191 bound DYRKs. (A) RMSD of pocket residues as a function of time. Average RMSDs and the respective standard deviations that are given in the plot were obtained for the last 40 ns of simulation time. (B) The distance between the Ca in the Gly-Glu residues of each DYRK (for DYRK1A: Gly168-Glu291; for DYRK1B: Gly120-Glu243) as a function of time. Average distance (and standard deviation) calculated after the first 100 ns of simulation time. (C) Time-averaged EDDA on DYRK1A and DYRK1B with AZ191 and the respective limits observed for each contribution. EDDA conducted on the larger subsystem B.

warrants caution when analysing MD results, we believe it underscores the previously noted differences in the accessibility of the catalytic lysine. This raises the question: how can two kinases that show such remarkable sequence and structural similarities exhibit such disparate behaviour on their ATP-binding pockets, allowing biological systems to selectively exploit kinase activity? Answer to this question, the long-range effect of distal residues, is corroborated by calculations (Table S8): as the number of protein atoms included in calculations increases, electrostatics become less repulsive. The impact of distal residues extends, however, to other interactions. The repulsion energy between the inhibitor and the protein increases with the pocket size. By including larger protein domains in the calculations, fine changes in the charge distribution and electronic populations occur, affecting how the two molecules interact. Note that because of the exponential decay of repulsion with distance, the 9 kcal/mol difference in repulsion implies only punctual modifications to the electronic densities. Overall, the calculations reveal a clear atomic mechanism underlying selectivity between the two kinases, which could only be uncovered by incorporating detailed electronic effects into the analysis.

3. Discussion

3.1. The challenge and rationale for DYRK1B selectivity

Developing selective DYRK1B inhibitors remains a significant challenge due to the high sequence and structural similarity within the CMGC kinase family. Most currently available compounds also potently inhibit closely related Homeodomain-Interacting Protein Kinases (HIPKs) and Cdc-like kinases (CLKs), both of which play essential roles in development and cell cycle regulation, raising potential toxicity concerns [48–51]. Achieving selectivity over these kinases is therefore critical for minimizing off-target effects and enabling a precise assessment of DYRK1B-dependent pathways.

Equally important is the ability to discriminate between DYRK1B and its closest paralog, DYRK1A. Despite their homology, the two kinases have distinct pathological roles. DYRK1B activity has been implicated in

tumor progression and non-alcoholic fatty liver disease, where its inhibition can trigger apoptosis [25,52]. However, concurrent inhibition of DYRK1A is undesirable due to the risk of elevated homocysteine levels known for their neurotoxic effects [53], as demonstrated in mice [54]. These findings underscore the need for *in vivo* testing of the benefits of selective DYRK kinase inhibition. Discovering the molecular and quantum-mechanical determinants that differentiate DYRK1A over DYRK1B can be exploited for rational drug design. Our work provides this important insight by presenting the first crystal structure of DYRK1B in complex with a potent inhibitor.

It is within this complex therapeutic landscape, where both the broad CMGC-family and specific DYRK1A off-target effects are potential liabilities, that our detailed structural analysis of DYRK1B provides a critical path forward. To understand the molecular basis for designing selective inhibitors, a direct comparative analysis of the two paralogs was essential.

3.2. A key technical insight for structure determination

A major barrier to the structural characterization of DYRK1B has been the difficulty in producing stable, homogenous protein. A key factor in successfully obtaining crystal structure of DYRK1B was therefore the isolation of a suitable protein sample. Our observation that the final, stable protein pool was completely phosphorylated, in contrast to the initial 14 % in the lysate, provides direct quantitative support for the model that inefficient folding and autophosphorylation are key bottlenecks for producing stable, recombinant human DYRK1B [42]. This suggests that the unphosphorylated or partially phosphorylated forms are indeed unstable and are selectively lost during purification, an insight that was instrumental to our success. Furthermore, the lower intrinsic thermal stability of mature DYRK1B compared to DYRK1A reported by Papenfuss et al. (2022) [42] is in excellent agreement with our own NanoDSF measurements (Tm of 47 °C *vs.* 56 °C, respectively).

3.3. Structural basis for paralog-specific inhibition

The enzyme-inhibitor interactions follow Koshland's induced fit model [55], where the binding of a ligand can induce conformational changes in the protein. To minimize inhibitor-induced variability in our comparative analysis, we therefore determined the structures of both DYRK1A and DYRK1B in complex with the same inhibitor, AZ191. Despite their high sequence homology and nearly identical ATP pockets, our integrated thermodynamic, structural, and computational analyses reveal that these similarities mask important energetic differences. The binding of harmine to both kinases is strongly enthalpically driven but incurs a large entropic penalty, consistent with its modest thermal stabilization effect (ΔTm of +1.0–2.5 °C). In stark contrast, AZ191 binding is more thermodynamically favorable, particularly for DYRK1A where it is driven by both enthalpy and entropy, and this correlates with a much greater thermal stabilization (ΔTm of +4.0–12.0 °C). The convergence of calorimetric, thermal-shift, and computational data confirms that, despite high structural homology, the active sites are not energetically equivalent, thereby providing a robust thermodynamic rationale for pursuing selectivity. This energetic divergence is likely rooted in specific structural features. Our comparative analysis highlights a single residue difference within the ATP pocket: a leucine in DYRK1A *versus* a methionine in DYRK1B. This site, addressed by the methoxy moiety of AZ191, suggests a convenient mechanism for enhancing specificity. Bulkier substituents are expected to cause a steric clash in DYRK1A due to the ramification in the leucine sidechain, a hypothesis that remains to be experimentally verified. Thus, optimizing interactions at this Leu/Met site appears to be one of the most direct rational approaches for enhancing the selectivity of small molecule inhibitors based on AZ191 or other scaffolds.

The quantum mechanical calculations revealed two additional factors that could be investigated to explore selectivity. Firstly, the ATP-binding pocket's electrostatic environment, influenced by distal residues, differs significantly between the kinases. However, leveraging electrostatics for selectivity is complex due to environmental factors like salt concentrations, which vary between *in vitro* and *in vivo* conditions. Secondly, simulations showed reduced accessibility to the catalytic lysine in DYRK1B, defined by a narrower ATP-binding pocket. This suggests a more stable and environment-independent approach for inhibitor design. Our model hypothesises that DYRK1B's restricted access to the catalytic lysine renders binding to this kinase less sensitive to the bulkiness of the lysine-binding groups. On the other hand, binding to DYRK1A should favour smaller and more compact lysine-binding groups. To test this, we examined published data on ligands structurally similar to AZ191, such as Abemaciclib and Cirtuvivint [32] (Fig. S14). The interaction with the catalytic lysine is key to both the inhibitors and involves a benzimidazole ring in Abemaciclib and a pyrazole ring in Cirtuvivint. Abemaciclib, which contains a bulky isopropyl group in its benzimidazole ring, shows a 5-fold higher affinity for DYRK1B than DYRK1A. Conversely, Cirtuvivint, with a smaller methyl group near the compact pyrazole ring, exhibits a 5-fold lower affinity for DYRK1B than DYRK1A. Additional evidence comes from ARN25067 and TCMDC-135051 [32] (Fig. S14), both with bulky substituents near the lysine-binding groups, resulting in a preference for DYRK1B (factor of 8 for ARN25067 and factor of 2 for TCMDC-135051). Similarly, compounds SM77 and SM330 [32] (Fig. S14) lack bulky substituents and bind more strongly to DYRK1A (factor of 2–3). EHT-1610, with its non-bulky methyl acetimidate group, also shows stronger binding to DYRK1A by a factor of 3 (Fig. S14). Our model also explains the slight preference of AZ191 for DYRK1B, given its indole ring's size in capturing the catalytic lysine.

In conclusion, our crystal structure of DYRK1B kinase opens the door for developing selective inhibitors. The almost identical ATP pockets of DYRK1A and DYRK1B underscore the challenge of this endeavour, but the Leu/Met site and the accessibility of the catalytic lysin offer potential anchor points. Guided by these structures, the development of selective inhibitors could enable formal testing of whether DYRK1B-specific targeting offers advantages over dual inhibition in certain disease models.

4. Experimental section

4.1. Compound purity

All compounds are >95 % pure by HPLC. Harmine, acquired from Sigma-Aldrich, catalog number 286044, purity of 98 %; AZ191, acquired from MedChemExpress, catalog number HY-12277, purity of 99.87 %.

4.2. Plasmid construction

The gene encoding the kinase domain of DYRK1B (78–442; Uniprot ID Q13627) was codon optimized, synthesized by Genscript and cloned into a pET24a plasmid. The kinase domain of DYRK1B was expressed with a C-terminal tobacco etch virus (TEV) protease cleavage site followed by His-Tag (ENLYFQ*GHHHHHH).

The gene fragment encoding the kinase domain of DYRK1A (126–490; Uniprot ID Q9Y463) was PCR amplified from plasmid pEXP17-DYRK1A [56] and subcloned into pET24a plasmid. The kinase domain of DYRK1A was expressed along with a non-cleavable C-terminal His-Tag.

4.3. Protein expression and purification

DYRK1B was expressed in *E. coli* LOBSTR strain (Kerafast) in TB medium supplemented with kanamycin (50 μg/ml) at 17 °C. Expression was induced at an OD600 = 0.8 using 0.5 mM IPTG. 16 h after the induction the cells were harvested by centrifugation and the pellet was resuspended in lysis buffer (20 mM HEPES pH 7.5, 300 mM NaCl, 5 %

glycerol, 15 mM imidazole, 5 mM $MgCl_2$, and 5 mM 2-mercaptoethanol) and lysed by sonication. Clarified lysate was incubated with HisPur™ Cobalt resin (ThermoFisher Scientific, Waltham, MA, United States) for 1 h at 4 °C, and DYRK1B was eluted with increments of imidazole concentration (50–300 mM). The elution fractions were pulled and dialyzed against 20 mM HEPES pH 7.5 containing 150 mM NaCl, 5 mM $MgCl_2$, 5 mM 2-mercaptoethanol and TEV protease. Released His-tag was removed by reverse chromatography on HisPur™ Cobalt resin. Final purification was obtained on HiLoad 16/600 Superdex 75 pg column (Cytiva) in 20 mM HEPES pH 7.5 containing 150 mM NaCl, 5 mM $MgCl_2$ and 1 mM TCEP. Noticing aggregation during expression, we tracked soluble *vs.* insoluble fractions, around 90 % of the protein was found in the insoluble fraction. From 6 L of culture, DYRK1B yield was 3 mg with purity >95 % as assessed by the SDS-PAGE.

The expression and initial purification steps for DYRK1A were identical to DYRK1B. Following cobalt affinity chromatography, the kinase was dialysed into 20 mM HEPES pH 7.5 containing 50 mM NaCl, 5 mM $MgCl_2$ and 5 mM 2-mercaptoethanol. Further purification was obtained by ion-exchange chromatography on HiTrap Q FF column (Cytiva) followed by size exclusion chromatography as for DYRK1B. From 6 L of culture, DYRK1A yield was 40 mg with purity >95 % as assessed by the SDS-PAGE.

Purified proteins were flash-frozen in liquid nitrogen and stored at −80 °C for further analysis.

4.4. Dye-based thermal shift assay

DYRK1A and DYRK1B kinase domain stability in the presence of harmine and AZ191 were analysed by the proteins' melting temperatures determination using Thermal Shift Assay (TSA) as described previously [57]. Both proteins were diluted to a final concentration of 1.5 mg/ml in TSA buffer consisting of 20 mM HEPES pH 8.0, 100 mM KCl, 10 mM $MgCl_2$, 1 mM 2-Mercaptoethanol. The assay mixture (total volume 25 µl per well) included 1× Sypro Orange dye (final dilution 1:200 from the 5000× stock; Invitrogen) and either the test compound (10 µM harmine or AZ191) or vehicle control (0.1 % DMSO). Samples were dispensed into a 96-well PCR plate, sealed to prevent evaporation, and subjected to a temperature gradient from 5 °C to 95 °C, increasing at a rate of 0.5 °C per minute, using a real-time PCR instrument with appropriate fluorescence detection settings (excitation at 492 nm, emission at 610 nm). Fluorescence intensity was recorded continuously as a function of temperature. The apparent protein melting temperature (T_m) was defined as the inflection point of the resulting fluorescence–temperature curve, corresponding to the maximum of the first derivative (–dF/dT).The experiment was carried out in triplicates repeated two times with similar results.

4.5. Cellular thermal shift assay (CETSA)

The interaction between AZ191 and full-length DYRK1B kinase was analysed by cellular thermal shift assay in complex cell lysate. Samples were prepared from control and inhibitor-exposed cell lysates. For each set, 2×10^7 cells were seeded in a 10-cm cultured dish. After 24 h of culturing, the cells were transfected with plasmid encoding Flag-DYRK1B using PEI Prime (Sigma-Aldrich), then 4 h later medium was changed and cells were left for 48 h. Then cells were treated with AZ191 (10 µM) or DMSO. 24 h later the cells were washed with PBS, treated with trypsin and collected by centrifugation at 1200 rpm for 5 min at room temperature. The pellets were gently resuspended in 800 µl of RIPA lysis buffer (Sigma-Aldrich) supplemented with Protease Inhibitor Cocktail (Roche) and disintegrated by sonication. The samples were centrifuged at 20000 rpm for 30 min at 4 °C, and the supernatants were transferred to new Eppendorf tubes. Pairs consisting of one control aliquot and one experimental aliquot were heated at 40 °C, 45 °C, 50 °C, 55 °C, 60 °C, 65 °C or 70 °C for 5 min. Next the samples were cooled on ice, centrifuged at 20000 rpm for 30 min at 4 °C and supernatants were analysed by Western Blot using monoclonal ANTI-FLAG M2-Peroxidase (HRP) antibody (Sigma-Aldrich, A8592). CETSA were performed in three independent biological replicates ($n = 3$); representative results are shown.

4.6. ADP-Glo kinase activity assay

The inhibitory potency (IC_{50}) of harmine and AZ191 was determined with the ADP-Glo kinase activity assay (Promega). The synthetic peptide DYRKtide (RRRFRPASPLRGPPK, Caslo ApS) was used as a substrate for DYRK1A and DYRK1B. 20 µl of kinase in reaction buffer (100 mM MOPS pH 6.8, 100 mM KCl, 10 mM $MgCl_2$) and 10 µl of compound were incubated for 15 min at room temperature. The reaction was started by simultaneous addition of 20 µl of substrates mix (ATP and DYRKtide) and continued for 30 min at room temperature. The 5 µl of reaction mixture was transformed to HTRF 96 well low volume plates (Cisbio) and the consumption of ATP was measured with ADP-Glo Kinase Assay kit (Promega Corporation) according to manufacturer protocol. The final composition of reaction reagents was - kinase (DYRK1A, DYRK1B) 5 ng/µl, compound (harmine, AZ191) 5 nM – 5 µM, ATP 100 µM and DYRKtide 400 µM. The ATP concentration was chosen based on the experimentally determined KM for DYRK1A and DYRK1B of 118 µM and 105 µM, respectively. All measurements were done in triplicate and repeated two times. The IC_{50} was determined using GraphPad Prism software.

4.7. Isothermal titration calorimetry measurements

ITC was performed with Nano ITC 2G (TA Instruments). To measure the DYRK1A interaction with harmine and AZ191, the proteins were dialyzed overnight at 4 °C against the ITC buffer (20 mM HEPES, 150 mM NaCl, 1 mM TCEP and 0.2 % DMSO). The reaction cell was filled with a respective protein solution (10 µM) whereas harmine or AZ191 was prepared in the same ITC buffer at 100 µM (from 50 mM stock solution) and loaded into a dosing syringe. All samples were degassed using an accessory degassing system (TA Instruments) prior to being placed in the ITC to minimize the possibility of gas bubble formation during the run by pulling a vacuum of 0.3–0.5 atm for 10–15 min. Each injection (5 µl) was performed in 300 s intervals. All experiments were conducted at 25 °C with a stirring rate of 250 rpm. The results were analysed using NanoAnalyze software (TA instruments). The experiment was carried out once for each independent protein purification (n = 3). Fig. 2D shows a representative titration.

4.8. NFAT translocation assay

HEK293T cells were maintained in Dulbecco's Modified Eagle Medium (DMEM) supplemented with 10 % fetal bovine serum (FBS) at 37 °C in a humidified incubator with 5 % CO_2. Cells were routinely tested and confirmed to be mycoplasma-free using a PCR-based detection method [58].

HEK293T cells were grown on µ-Slide 8 well (IBIDI) to 50 %–70 % confluency. The plasmids expressing mCherry-DYRK1B and eGFP-NFATc1 were transiently co-transfected for 48 h with PEI Prime transfection reagent (Sigma-Aldrich) at a PEI:DNA ratio of 3:1 (*w*/w). For each well, 0.75 µg total plasmid DNA was diluted in Opti-MEM and mixed with 2.25 µg PEI Prime, incubated at room temperature for 15 min, and added dropwise to the cells. The expression was allowed to proceed for 48 h. Cells were pre-treated with inhibitor AZ191 (10 µM) or DMSO (vehicle control, 0.1 %) for 3 h and then stimulated with ionomycin (1 µM, Thermo Fisher Scientific) for 1 h to induce NFAT nuclear translocation. Cells were washed with 1 ml PBS and the nuclei were stained with Hoechst 33258 (1 µg/ml, ThermoScientific) for 10 min at 37 °C and fixed with 4 % paraformaldehyde in phosphate-buffered saline (PBS) for 10 min at 25 °C. Images were collected with Zeiss Axio Observer 3 fluorescence microscope and analysed in ZEN Blue edition

software.

4.9. Mass spectrometry

Samples for MS were taken during first step of protein purification (after sonication) and final purified protein. Bottom-up protein identification with phospho-modified residues was done according to the typically used protocols. Briefly, sample in the form of Coomassie Brillant Blue stained band was excised and destained (ammonia-bicarbonate/AMBIC buffer 50 mM, pH = 8.0/acetonitrile). Then the band was rehydrated in the AMBIC buffer with following routine reduction (5 mM DTT, 10 min, 80 °C, with shaking) and cysteine alkylation (5 mM iodoacetamide, 10 min, 80 °C, with shaking) procedure. Peptides were eluted from the gel, using water/acetonitrile/formic acid mixture (9/10/1 *v*/v/v), then freeze-dried and dissolved in the 60 μl of 4 % acetontrile/water solution supplemented with 0.1 % formic acid. 5 μl were introduced into the nanoLC-MS/MS system. Equipment used: nanoLC: Ultimate 3000 (Thermo, Bremen, Germany) in the set-up containing trap cartridge (Acclaim Pepmap 100, C18, 1 mm ID, 5 mm length, particle size 5 μm) and analytical column (Acclaim Pepmap 100, C18, 75 μm ID, 150 mm length, particle size 3 μm). Mass spectrometer: Exploris 240 (Thermo, Bremen, Germany) equipped with Nanopray FLEX ion source. Peptides separation was done using following solvents: A: water+0.1 % formic acid, B: acetonitrile +0.1 % formic acid. Gradient settings: $T = 0$ min 5 %B, $T = 5$ min 5 %B, $T = 20$ min 35 %B, $T = 22$ min 75 %B, $T = 23$ min 75 %B, $T = 25$ min 5 %B, $T = 30$ min 5 %B. Mass spectrometer settings: MS spectrum range: 350–1600 *m/z*, resolution 30,000, MS/MS spectrum range: 200–2000 m/z, resolution 60,000. Up to 6 fragmentation scans between MS scans. Ion exclusion for 20 s after 2 MS/MS scans.

Data analysis was done as follows: conversion from raw to mgf files was done with the aid of RawConverter software, ver. 1.1.0.23 64-bit (from: http://fields.scripps.edu/rawconv/). Mgf files were searched against the database containing the single sequence of the protein-of-interest (DYR1B_HUMAN). Search engine was the local Mascot server, ver. 2.8.0 (Matrixscience, UK). Mascot settings were as follows: enzyme: trypsin, up to 2 missed cleavages; fixed modifications: carbamidomethylation; variable modifications: Met-oxidation, phospho (ST), phospho (Y); MS and MS/MS tolerances: 100 ppm; #13C = 1; peptide charge: 2+, 3+ and 4+; instrument: ESI-FTICR.

4.10. Protein crystallization, data collection and structure determination

DYRK1B was concentrated to 10–13 mg/ml and incubated overnight with 5-M excess of AZ191 at 4 °C. For crystallization condition screening the preparation was mixed 1:1 (*v*/v) with crystallization solutions. The experiments were carried out at 20 °C and crystals appeared within 1–3 days. The best crystals were obtained using sitting drop vapor diffusion setup in 0.1 M Bis-Tris pH 5.5 containing 25 % PEG 3350, 0.2 M magnesium chloride and 0.1 M manganese chloride. Crystals of DYRK1A in complex with AZ191 were obtained in a manner similar to those of DYRK1B, but from 0.1 M HEPES pH 7.5 containing 10 % PEG 8000, 8 % ethylene glycol and 0.1 M ammonium sulfate. Crystals were cryoprotected in mother liquor containing 25 % ethylene glycol and flash-frozen in liquid nitrogen.

X-ray diffraction data were collected at BESSY (Berlin) and DESY (Hamburg). The diffraction data was indexed and integrated using XDS [59]. Data was scaled in AIMLESS [60] from the CCP4 software package [61]. Following steps were performed in Phenix [62]. The structures of DYRK1B and DYRK1A were solved by molecular replacement using PHASER [63] and respective search models: processed AlphaFold model AF-Q9Y463-F1 and PDB ID 7A4O. Models were refined by interchanging cycles of automated refinement using phenix.refine [64] and manual building in Coot [65]. Restraints for the inhibitor were created in Grade Web Server [66].

4.11. Computational methods

Energy Decomposition and Deconvolutional Analysis (EDDA) calculations were performed using our in-house quantum chemical package, ULYSSES [67]. Details of the EDDA method were published earlier [45,68]. The quantum chemical method of choice was GFN2-xTB [69] with ALPB aqueous solvation [70]. Molecular Dynamics simulations were conducted using GROMACS [71] with OPLS [72–74] and CHARMM36 [75] force fields. Explicit water was simulated using the TIP3P model [76,77]. Simulations were conducted following standard protocols [78] in the NPT ensemble. Temperature and density were controlled over all stages to ensure stability of the simulations. Apo protein simulations were run for 500 ns, whereas kinase and ligand systems were simulated for 100 ns. Preparation of the protein for EDDA calculations was done using Chimera [79].

4.12. Figures

Figures were prepared in ChimeraX (ver. 1.10) [80,81], IBS 2.0 [82] and GIMP (ver. 2.10.36).

4.13. Limitations of the study

While our findings provide new structural and mechanistic insights into DYRK1B selectivity, several limitations must be acknowledged. First, our analyses were focused on a limited chemotypes (Harmine and AZ191), and it remains to be determined whether other chemotypes exploit the same determinants. Similarly, the crystallographic structures represent static conformations obtained under specific conditions, which may not fully capture the conformational heterogeneity of the kinases in solution or in the cellular environment. Computational predictions of electronic interactions and lysine accessibility provide valuable mechanistic hypotheses that could further benefit by a larger kinase-inhibitor interaction library. Finally, while our biochemical and cellular assays strongly support the mechanistic conclusions, broader kinome profiling and *in vivo* studies will be needed to fully evaluate the therapeutic potential. Together, these considerations do not detract from the significance of the current findings, rather outline the next steps.

CRediT authorship contribution statement

Przemyslaw Grygier: Writing – review & editing, Writing – original draft, Visualization, Methodology, Investigation, Conceptualization. **Katarzyna Pustelny:** Writing – review & editing, Writing – original draft, Visualization, Methodology, Investigation, Funding acquisition, Conceptualization. **Filipe Menezes:** Writing – review & editing, Writing – original draft, Visualization, Methodology, Investigation, Conceptualization. **Malgorzata Jemiola-Rzeminska:** Validation, Methodology, Investigation. **Piotr Suder:** Visualization, Methodology, Investigation. **Grzegorz Dubin:** Writing – review & editing, Writing – original draft. **Anna Czarna:** Writing – review & editing, Writing – original draft, Supervision, Project administration, Methodology, Investigation, Funding acquisition, Conceptualization.

PDB ID codes

Crystal structures of DYRK1B and DYRK1A in complex with AZ191 described in this manuscript are available in PDB (Protein Data Bank; https://www.rcsb.org/) with ID's 8C2Z and 8C3G, respectively.

Declaration of competing interest

The authors declare that they have no known competing financial interests or personal relationships that could have appeared to influence the work reported in this paper.

Acknowledgements

This work was supported by a grant from National Science Centre (2019/34/E/NZ1/00467 and 2022/45/B/NZ7/04269) to AC and (2022/06/X/NZ1/01418) to KP, respectively, and by NAWA Polish Returns 2018 (PPN/PPO/2018/1/00046/U/00001) to AC. We extend our gratitude to Grzegorz Popowicz (Institute of Structural Biology, Helmholtz Zentrum Munchen, Neuherberg, Germany) for his invaluable support, guidance, and scholarly discussions throughout the project. We acknowledge the MCB Structural Biology Core Facility (supported by the TEAM TECH CORE FACILITY/2017-4/6 grant from the Foundation for Polish Science) for valuable support. X-ray data were collected at the HZB BESSY II 14.1 and P11 at DESY. We thank HZB for the allocation of neutron/synchrotron radiation beamtime. We acknowledge DESY (Hamburg, Germany), a member of the Helmholtz Association HGF, for the provision of experimental facilities. Parts of this research were carried out at PETRA III and we would like to thank Johanna Hakanpää for assistance in using beamline P11. Beamtime was allocated for proposal I-20220342 EC.

Appendix A. Supplementary data

MS/MS spectra of DYRK1B

DYRK1B MS/MS data, crystallographic data, CETSA assay, quantum chemical calculations, additional interaction maps, additional molecular modelling data (PDF) Supplementary data to this article can be found online at https://doi.org/10.1016/j.ijbiomac.2025.148124.

Data availability

Data will be made available on request.

References

[1] L.J. Wilson, A. Linley, D.E. Hammond, F.E. Hood, J.M. Coulson, D.J. MacEwan, S. J. Ross, J.R. Slupsky, P.D. Smith, P.A. Eyers, I.A. Prior, New perspectives, opportunities, and challenges in exploring the human protein kinome, Cancer Res. 78 (2018) 15–29, https://doi.org/10.1158/0008-5472.CAN-17-2291.

[2] G. Manning, D.B. Whyte, R. Martinez, T. Hunter, S. Sudarsanam, The protein kinase complement of the human genome, Science 298 (2002) (1979) 1912–1934, https://doi.org/10.1126/science.1075762.

[3] M.M. Attwood, D. Fabbro, A.V. Sokolov, S. Knapp, H.B. Schiöth, Trends in kinase drug discovery: targets, indications and inhibitor design, Nat. Rev. Drug Discov. (2021) 839–861, https://doi.org/10.1038/s41573-021-00252-y, 2021 20:11 20.

[4] S. Aranda, A. Laguna, S. de la Luna, DYRK family of protein kinases: evolutionary relationships, biochemical properties, and functional roles, FASEB J. 25 (2011) 449–462, https://doi.org/10.1096/FJ.10-165837.

[5] H. Kentrup, W. Becker, J. Heukelbach, A. Wilmes, A. Schürmann, C. Huppertz, H. Kainulainen, H.G. Joost, Dyrk, a dual specificity protein kinase with unique structural features whose activity is dependent on tyrosine residues between subdomains VII and VIII, J. Biol. Chem. 271 (1996) 3488–3495, https://doi.org/10.1074/jbc.271.7.3488.

[6] W. Becker, H.G. Joost, Structural and functional characteristics of Dyrk, a novel subfamily of protein kinases with dual specificity, Prog. Nucleic Acid Res. Mol. Biol. 62 (1998) 1–17, https://doi.org/10.1016/S0079-6603(08)60503-6.

[7] E. Deboever, A. Fistrovich, C. Hulme, T. Dunckley, The Omnipresence of DYRK1A in Human Diseases, Int. J. Mol. Sci. 23 (2022), https://doi.org/10.3390/IJMS23169355. Page 9355 23 (2022) 9355.

[8] J. Wegiel, C.X. Gong, Y.W. Hwang, The role of DYRK1A in neurodegenerative diseases, FEBS J. 278 (2011) 236–245, https://doi.org/10.1111/J.1742-4658.2010.07955.X.

[9] T. Liu, Y. Wang, J. Wang, C. Ren, H. Chen, J. Zhang, DYRK1A inhibitors for disease therapy: current status and perspectives, Eur. J. Med. Chem. 229 (2022) 114062, https://doi.org/10.1016/J.EJMECH.2021.114062.

[10] R. Abbassi, T.G. Johns, M. Kassiou, L. Munoz, DYRK1A in neurodegeneration and cancer: molecular basis and clinical implications, Pharmacol. Ther. 151 (2015) 87–98, https://doi.org/10.1016/J.PHARMTHERA.2015.03.004.

[11] M. Álvarez, X. Estivill, S. de la Luna, DYRK1A accumulates in splicing speckles through a novel targeting signal and induces speckle disassembly, J. Cell Sci. 116 (2003) 3099–3107, https://doi.org/10.1242/JCS.00618.

[12] S.J. Davis, K.E. Sheppard, R.B. Pearson, I.G. Campbell, K.L. Gorringe, K.J. Simpson, Functional analysis of genes in regions commonly amplified in high-grade serous and endometrioid ovarian cancer, Clin. Cancer Res. 19 (2013) 1411–1421, https://doi.org/10.1158/1078-0432.CCR-12-3433/85792/AM/FUNCTIONAL-ANALYSIS-OF-GENES-IN-REGIONS-COMMONLY.

[13] R. Kuuselo, R. Simon, R. Karhu, P. Tennstedt, A.H. Marx, J.R. Izbicki, E. Yekebas, G. Sauter, A. Kallioniemi, 19q13 amplification is associated with high grade and stage in pancreatic cancer, Genes Chromosom. Cancer 49 (2010) 569–575, https://doi.org/10.1002/GCC.20767.

[14] W. Becker, A wake-up call to quiescent cancer cells – potential use of DYRK1B inhibitors in cancer therapy, FEBS J. 285 (2018) 1203–1211, https://doi.org/10.1111/FEBS.14347;JOURNAL:JOURNAL:14321033.

[15] E. Friedman, The Kinase Mirk/dyrk1B: A Possible Therapeutic Target in Pancreatic Cancer, Cancers 2 (2010) 1492–1512, https://doi.org/10.3390/CANCERS2031492. Pages 1492–1512 2 (2010).

[16] J. Hu, H. Nakhla, E. Friedman, Transient arrest in a quiescent state allows ovarian cancer cells to survive suboptimal growth conditions and is mediated by both Mirk/dyrk1b and p130/Rb2, Int. J. Cancer 129 (2011) 307–318, https://doi.org/10.1002/IJC.25692.

[17] J. Gao, X. Yang, P. Yin, W. Hu, H. Liao, Z. Miao, C. Pan, N. Li, The involvement of FoxO in cell survival and chemosensitivity mediated by Mirk/Dyrk1B in ovarian cancer, Int. J. Oncol. 40 (2012) 1203–1209, https://doi.org/10.3892/IJO.2011.1293.

[18] E. Friedman, Mirk/dyrk1B Kinase in Ovarian Cancer, Int. J. Mol. Sci. 14 (2013) 5560–5575, 14 (2013) 5560–5575, https://doi.org/10.3390/IJMS14035560.

[19] J. Gao, Z. Zheng, B. Rawal, M.J. Schell, G. Bepler, E.B. Haura, Mirk/Dyrk1B, a novel therapeutic target, mediates cell survival in non-small cell lung cancer cells, Cancer Biol. Ther. 8 (2009) 1671–1679, https://doi.org/10.4161/CBT.8.17.9322.

[20] Y. Chen, S. Wang, Z. He, F. Sun, Y. Huang, Q. Ni, H. Wang, Y. Wang, C. Cheng, Dyrk1B overexpression is associated with breast cancer growth and a poor prognosis, Hum. Pathol. 66 (2017) 48–58, https://doi.org/10.1016/J.HUMPATH.2017.02.033.

[21] X. Deng, D.Z. Ewton, S. Li, A. Naqvi, S.E. Mercer, S. Landas, E. Friedman, The kinase Mirk/Dyrk1B mediates cell survival in pancreatic ductal adenocarcinoma, Cancer Res. 66 (2006) 4149–4158, https://doi.org/10.1158/0008-5472.CAN-05-3089.

[22] S.E. Mercer, D.Z. Ewton, S. Shah, A. Naqvi, E. Friedman, Mirk/Dyrk1b mediates cell survival in rhabdomyosarcomas, Cancer Res. 66 (2006) 5143–5150, https://doi.org/10.1158/0008-5472.CAN-05-1539.

[23] X. Deng, S.E. Mercer, C.Y. Sun, E. Friedman, The normal function of the cancer kinase Mirk/dyrk1B is to reduce reactive oxygen species, Genes Cancer 5 (2014) 22–30, https://doi.org/10.18632/GENESANDCANCER.1.

[24] H. Chen, J. Shen, E. Choy, F.J. Hornicek, A. Shan, Z. Duan, H. Chen, J. Shen, E. Choy, F.J. Hornicek, A. Shan, Z. Duan, Targeting DYRK1B suppresses the proliferation and migration of liposarcoma cells, Oncotarget 9 (2017) 13154–13166, https://doi.org/10.18632/ONCOTARGET.22743.

[25] J. Hu, H. Deng, E.A. Friedman, Ovarian cancer cells, not normal cells, are damaged by Mirk/Dyrk1B kinase inhibition, Int. J. Cancer 132 (2013) 2258–2269, https://doi.org/10.1002/IJC.27917.

[26] A. Barzowska, B. Pucelik, K. Pustelny, A. Matsuda, A. Martyniak, J. Stępniewski, A. Maksymiuk, M. Dawidowski, U. Rothweiler, J. Dulak, G. Dubin, A. Czarna, DYRK1A kinase inhibitors promote β-cell survival and insulin homeostasis, Cells 10 (2021) 2263, https://doi.org/10.3390/CELLS10092263/S1.

[27] K. Kumar, C. Suebsuwong, P. Wang, A. Garcia-Ocana, A.F. Stewart, R.J. Devita, DYRK1A inhibitors as potential therapeutics for β-cell regeneration for diabetes, J. Med. Chem. 64 (2021) 2901–2922, https://doi.org/10.1021/ACS.JMEDCHEM.0C02050/ASSET/IMAGES/MEDIUM/JM0C02050_0013.GIF.

[28] P. Wang, E. Karakose, L. Choleva, K. Kumar, R.J. DeVita, A. Garcia-Ocaña, A. F. Stewart, Human beta cell regenerative drug therapy for diabetes: past achievements and future challenges, Front Endocrinol (Lausanne) 12 (2021) 671946, https://doi.org/10.3389/FENDO.2021.671946/BIBTEX.

[29] C. Ackeifi, E. Swartz, K. Kumar, H. Liu, S. Chalada, E. Karakose, D.K. Scott, A. Garcia-Ocaña, R. Sanchez, R.J. DeVita, A.F. Stewart, P. Wang, Pharmacologic and genetic approaches define human pancreatic β cell mitogenic targets of DYRK1A inhibitors, JCI Insight 5 (2020), https://doi.org/10.1172/JCI.INSIGHT.132594.

[30] D. Frost, B. Meechoovet, T. Wang, S. Gately, M. Giorgetti, I. Shcherbakova, T. Dunckley, β-Carboline compounds, including Harmine, inhibit DYRK1A and tau phosphorylation at multiple Alzheimer's disease-related sites, PLoS One 6 (2011) e19264, https://doi.org/10.1371/JOURNAL.PONE.0019264.

[31] P. Wang, J.C. Alvarez-Perez, D.P. Felsenfeld, H. Liu, S. Sivendran, A. Bender, A. Kumar, R. Sanchez, D.K. Scott, A. Garcia-Ocaña, A.F. Stewart, A high-throughput chemical screen reveals that harmine-mediated inhibition of DYRK1A increases human pancreatic beta cell replication, Nat. Med. 21 (4) (2015) 383–388, https://doi.org/10.1038/nm.3820, 21 (2015).

[32] M.F. Lindberg, E. Deau, J. Arfwedson, N. George, P. George, P. Alfonso, A. Corrionero, L. Meijer, Comparative efficacy and selectivity of pharmacological inhibitors of DYRK and CLK protein kinases, J. Med. Chem. 66 (2023) 4106–4130, https://doi.org/10.1021/acs.jmedchem.2c02068.

[33] D. Bossemeyer, The glycine-rich sequence of protein kinases: a multifunctional element, Trends Biochem. Sci. 19 (1994) 201–205, https://doi.org/10.1016/0968-0004(94)90022-1.

[34] S.R. Hubbard, Crystal structure of the activated insulin receptor tyrosine kinase in complex with peptide substrate and ATP analog, EMBO J. 16 (1997) 5572–5581, https://doi.org/10.1093/EMBOJ/16.18.5572.

[35] D.K. Treiber, N.P. Shah, Ins and outs of kinase DFG motifs, Chem. Biol. 20 (2013) 745–746, https://doi.org/10.1016/J.CHEMBIOL.2013.06.001.

[36] M. Soundararajan, A.K. Roos, P. Savitsky, P. Filippakopoulos, A.N. Kettenbach, J. V. Olsen, S.A. Gerber, J. Eswaran, S. Knapp, J.M. Elkins, Structures of down syndrome kinases, DYRKs, reveal mechanisms of kinase activation and substrate

recognition, Structure 21 (2013) 986–996, https://doi.org/10.1016/j.str.2013.03.012.
[37] S. Abu Jhaisha, E.W. Widowati, I. Kii, R. Sonamoto, S. Knapp, C. Papadopoulos, W. Becker, DYRK1B mutations associated with metabolic syndrome impair the chaperone-dependent maturation of the kinase domain, Sci. Rep. (2017) 1–13, https://doi.org/10.1038/s41598-017-06874-w, 7:1 7 (2017).
[38] M. Rechsteiner, S.W. Rogers, PEST sequences and regulation by proteolysis, Trends Biochem. Sci. 21 (1996) 267–271, https://doi.org/10.1016/S0968-0004(96)10031-1.
[39] A.L. Ashford, D. Oxley, J. Kettle, K. Hudson, S. Guichard, S.J. Cook, P.A. Lochhead, A novel DYRK1B inhibitor AZ191 demonstrates that DYRK1B acts independently of GSK3β to phosphorylate cyclin D1 at Thr286, not Thr288, Biochem. J. 457 (2014) 43–56, https://doi.org/10.1042/BJ20130461.
[40] S. Himpel, P. Panzel, K. Eirmbter, H. Czajkowska, M. Sayed, L.C. Packman, T. Blundell, H. Kentrup, J. Grötzinger, H.-G. Joost, W. Becker, Identification of the autophosphorylation sites and characterization of their effects in the protein kinase DYRK1A, Biochem. J. 359 (2001) 497–505, https://doi.org/10.1042/BJ3590497.
[41] W. Becker, W. Sippl, Activation, regulation, and inhibition of DYRK1A, FEBS J. 278 (2011) 246–256, https://doi.org/10.1111/J.1742-4658.2010.07956.X.
[42] M. Papenfuss, S. Lützow, G. Wilms, A. Babendreyer, M. Flaßhoff, C. Kunick, W. Becker, Differential maturation and chaperone dependence of the paralogous protein kinases DYRK1A and DYRK1B, Sci. Rep. 12 (2022) 1–15, https://doi.org/10.1038/s41598-022-06423-0, 1 12 (2022).
[43] Y. Zeng, Y. Wang, Z. Wu, K. Kang, X. Peng, W. Peng, J. Qu, L. Liu, J. Usha Raj, D. Gou, Mir-9 enhances the transactivation of nuclear factor of activated T cells by targeting KPNB1 and DYRK1B, Am. J. Phys. Cell Physiol. 308 (2015) C720–C728, https://doi.org/10.1152/AJPCELL.00299.2014/ASSET/IMAGES/LARGE/ZH00091577220007.JPEG.
[44] V. Alexandrov, M. Vilenchik, O. Kantidze, N. Tsutskiridze, D. Kharchilava, P. Lhewa, A. Shishkin, Y. Gankin, A. Kirpich, Novel efficient multistage Lead optimization pipeline experimentally validated for DYRK1B selective inhibitors, J. Med. Chem. 65 (2022) 13784–13792, https://doi.org/10.1021/acs.jmedchem.2c00988.
[45] P. Grygier, K. Pustelny, J. Nowak, P. Golik, G.M. Popowicz, O. Plettenburg, G. Dubin, F. Menezes, A. Czarna, Silmitasertib (CX-4945), a clinically used CK2-kinase inhibitor with additional effects on GSK3β and DYRK1A kinases: a structural perspective, J. Med. Chem. 66 (2023) 4009–4024, https://doi.org/10.1021/acs.jmedchem.2c01887.
[46] C. Discovery, J. Boitreaud, J. Dent, M. McPartlon, J. Meier, V. Reis, A. Rogozhnikov, K. Wu, Chai-1: decoding the molecular interactions of life, BioRxiv (2024), https://doi.org/10.1101/2024.10.10.615955, 2024.10.10.615955.
[47] Y. Ogawa, Y. Nonaka, T. Goto, E. Ohnishi, T. Hiramatsu, I. Kii, M. Yoshida, T. Ikura, H. Onogi, H. Shibuya, T. Hosoya, N. Ito, M. Hagiwara, Development of a novel selective inhibitor of the Down syndrome-related kinase Dyrk1A, Nat. Commun. (2010) 1–9, https://doi.org/10.1038/ncomms1090, 1:1 1 (2010).
[48] J. Chen, E.M. Verheyen, Homeodomain-interacting protein kinase regulates yorkie activity to promote tissue growth, Curr. Biol. 22 (2012) 1582–1586, https://doi.org/10.1016/j.cub.2012.06.074.
[49] S.J.H. Wang, D.A.R. Sinclair, H.Y. Kim, S.D. Kinsey, B. Yoo, C.R.Y. Shih, K.K. L. Wong, C. Krieger, N. Harden, E.M. Verheyen, Homeodomain-interacting protein kinase (Hipk) plays roles in nervous system and muscle structure and function, PLoS One 15 (2020) e0221006, https://doi.org/10.1371/JOURNAL.PONE.0221006.
[50] D. Dominguez, Y.H. Tsai, R. Weatheritt, Y. Wang, B.J. Blencowe, Z. Wang, An extensive program of periodic alternative splicing linked to cell cycle progression, Elife 5 (2016), https://doi.org/10.7554/ELIFE.10288.
[51] M. Muraki, B. Ohkawara, T. Hosoya, H. Onogi, J. Koizumi, T. Koizumi, K. Sumi, J. I. Yomoda, M.V. Murray, H. Kimura, K. Furuichi, H. Shibuya, A.R. Krainer, M. Suzuki, M. Hagiwara, Manipulation of alternative splicing by a newly developed inhibitor of Clks, J. Biol. Chem. 279 (2004) 24246–24254, https://doi.org/10.1074/jbc.M314298200.
[52] N. Bhat, A. Narayanan, M. Fathzadeh, M. Kahn, D. Zhang, L. Goedeke, A. Neogi, R. L. Cardone, R.G. Kibbey, C. Fernandez-Hernando, H.N. Ginsberg, D. Jain, G. I. Shulman, A. Mani, Dyrk1b promotes hepatic lipogenesis by bypassing canonical insulin signaling and directly activating mTORC2 in mice, J. Clin. Invest. 132 (2022), https://doi.org/10.1172/JCI153724.
[53] Y. Jang, H.-J. Kim, Y.H. Kwon, The involvement of calpain in homocysteine-induced apoptosis in SH-SY5Y cells, FASEB J. 22 (2008) 877.3-877, https://doi.org/10.1096/FASEBJ.22.1_SUPPLEMENT.877.3.
[54] C. Noll, C. Planque, C. Ripoll, F. Guedj, A. Diez, V. Ducros, N. Belin, A. Duchon, J. L. Paul, A. Badel, B. de Freminville, Y. Grattau, H. Bléhaut, Y. Herault, N. Janel, J. M. Delabar, DYRK1A, a novel determinant of the methionine-homocysteine cycle in different mouse models overexpressing this Down-syndrome-associated kinase, PLoS One 4 (2009) e7540, https://doi.org/10.1371/JOURNAL.PONE.0007540.
[55] D.E. Koshland, Application of a theory of enzyme specificity to protein synthesis, Proc. Natl. Acad. Sci. 44 (1958) 98–104, https://doi.org/10.1073/pnas.44.2.98.
[56] A. Czarna, J. Wang, D. Zelencova, Y. Liu, X. Deng, H.G. Choi, T. Zhang, W. Zhou, J. W. Chang, H. Kildalsen, O.M. Seternes, N.S. Gray, R.A. Engh, U. Rothweiler, Novel scaffolds for dual specificity tyrosine-phosphorylation-regulated kinase (DYRK1A) inhibitors, J. Med. Chem. 61 (2018) 7560–7572, https://doi.org/10.1021/acs.jmedchem.7b01847.
[57] L. Reinhard, H. Mayerhofer, A. Geerlof, J. Mueller-Dieckmann, M.S. Weiss, Optimization of protein buffer cocktails using Thermofluor, Acta Crystallogr. Sect. F 69 (2013) 209–214, https://doi.org/10.1107/S1744309112051858.
[58] D. Siegl, M. Kruchem, S. Jansky, E. Eichler, D. Thies, U. Hartwig, D. Schuppan, E. Bockamp, A PCR protocol to establish standards for routine mycoplasma testing that by design detects over ninety percent of all known mycoplasma species, IScience 26 (2023), https://doi.org/10.1016/j.isci.2023.106724.
[59] W. Kabsch, XDS, Acta Crystallogr D Struct Biol 66 (2010) 125–132, https://doi.org/10.1107/S0907444909047337.
[60] P.R. Evans, G.N. Murshudov, How good are my data and what is the resolution? Acta Crystallogr D Struct Biol 69 (2013) 1204–1214, https://doi.org/10.1107/S0907444913000061.
[61] J. Agirre, M. Atanasova, H. Bagdonas, C.B. Ballard, A. Baslé, J. Beilsten-Edmands, R.J. Borges, D.G. Brown, J.J. Burgos-Mármol, J.M. Berrisford, P.S. Bond, I. Caballero, L. Catapano, G. Chojnowski, A.G. Cook, K.D. Cowtan, T.I. Croll, J. Debreczeni, N.E. Devenish, E.J. Dodson, T.R. Drevon, P. Emsley, G. Evans, P. R. Evans, M. Fando, J. Foadi, L. Fuentes-Montero, E.F. Garman, M. Gerstel, R. J. Gildea, K. Hatti, M.L. Hekkelman, P. Heuser, S.W. Hoh, M.A. Hough, H. T. Jenkins, E. Jiménez, R.P. Joosten, R.M. Keegan, N. Keep, E.B. Krissinel, P. Kolenko, O. Kovalevskiy, V.S. Lamzin, D.M. Lawson, A.A. Lebedev, A.G. W. Leslie, B. Lohkamp, F. Long, M. Malý, A.J. McCoy, S.J. McNicholas, A. Medina, C. Millán, J.W. Murray, G.N. Murshudov, R.A. Nicholls, M.E.M. Noble, R. Oeffner, N.S. Pannu, J.M. Parkhurst, N. Pearce, J. Pereira, A. Perrakis, H.R. Powell, R. J. Read, D.J. Rigden, W. Rochira, M. Sammito, F. Sánchez Rodríguez, G. M. Sheldrick, K.L. Shelley, F. Simkovic, A.J. Simpkin, P. Skubak, E. Sobolev, R. A. Steiner, K. Stevenson, I. Tews, J.M.H. Thomas, A. Thorn, J.T. Valls, V. Uski, I. Usón, A. Vagin, S. Velankar, M. Vollmar, H. Walden, D. Waterman, K.S. Wilson, M.D. Winn, G. Winter, M. Wojdyr, K. Yamashita, The CCP4 suite: integrative software for macromolecular crystallography, Acta Crystallogr. D Struct. Biol. 79 (2023) 449–461, https://doi.org/10.1107/S2059798323003595.
[62] D. Liebschner, P.V. Afonine, M.L. Baker, G. Bunkoczi, V.B. Chen, T.I. Croll, B. Hintze, L.W. Hung, S. Jain, A.J. McCoy, N.W. Moriarty, R.D. Oeffner, B.K. Poon, M.G. Prisant, R.J. Read, J.S. Richardson, D.C. Richardson, M.D. Sammito, O. V. Sobolev, D.H. Stockwell, T.C. Terwilliger, A.G. Urzhumtsev, L.L. Videau, C. J. Williams, P.D. Adams, Macromolecular structure determination using X-rays, neutrons and electrons: recent developments in Phenix, Acta Crystallogr D Struct Biol 75 (2019) 861–877, https://doi.org/10.1107/S2059798319011471.
[63] A.J. McCoy, R.W. Grosse-Kunstleve, P.D. Adams, M.D. Winn, L.C. Storoni, R. J. Read, Phaser crystallographic software, J. Appl. Crystallogr. 40 (2007) 658–674, https://doi.org/10.1107/S0021889807021206.
[64] P.V. Afonine, R.W. Grosse-Kunstleve, N. Echols, J.J. Headd, N.W. Moriarty, M. Mustyakimov, T.C. Terwilliger, A. Urzhumtsev, P.H. Zwart, P.D. Adams, Towards automated crystallographic structure refinement with phenix.refine, Acta Crystallogr D Struct Biol 68 (2012) 352–367, https://doi.org/10.1107/S0907444912001308.
[65] P. Emsley, B. Lohkamp, W.G. Scott, K. Cowtan, Features and development of coot, Acta Crystallogr. D. Struct. Biol. 66 (2010) 486–501, https://doi.org/10.1107/S0907444910007493.
[66] O.S. Smart, A. Sharff, J. Holstein, T.O. Womack, C. Flensburg, P. Keller, W. Paciorek, C. Vonrhein, G. Bricogne, Grade2 version 1.3.0, Global Phasing Ltd, Cambridge, United Kingdom, 2021.
[67] F. Menezes, G.M. Popowicz, ULYSSES: an efficient and easy to use Semiempirical library for C++, J. Chem. Inf. Model. 62 (2022) 3685–3694, https://doi.org/10.1021/acs.jcim.2c00757.
[68] F. Menezes, T. Fröhlich, G.M. Popowicz, Can quantum chemistry improve the understanding of protein-ligand interactions? Implications for structure based drug Discovery, BioRxiv (2023), https://doi.org/10.1101/2023.06.01.543295, 2023.06.01.543295.
[69] C. Bannwarth, S. Ehlert, S. Grimme, GFN2-xTB - an accurate and broadly parametrized self-consistent tight-binding quantum chemical method with multipole electrostatics and density-dependent dispersion contributions, J. Chem. Theory Comput. 15 (2019) 1652–1671, https://doi.org/10.1021/acs.jctc.8b01176.
[70] S. Ehlert, M. Stahn, S. Spicher, S. Grimme, Robust and efficient implicit solvation model for fast semiempirical methods, J. Chem. Theory Comput. 17 (2021) 4250–4261, https://doi.org/10.1021/acs.jctc.1c00471.
[71] M.J. Abraham, T. Murtola, R. Schulz, S. Páll, J.C. Smith, B. Hess, E. Lindah, Gromacs: high performance molecular simulations through multi-level parallelism from laptops to supercomputers, SoftwareX 1–2 (2015) 19–25, https://doi.org/10.1016/j.softx.2015.06.001.
[72] W.L. Jorgensen, J. Tirado-Rives, Potential energy functions for atomic-level simulations of water and organic and biomolecular systems, Proc. Natl. Acad. Sci. USA 102 (2005) 6665–6670, https://doi.org/10.1073/pnas.0408037102.
[73] L.S. Dodda, J.Z. Vilseck, J. Tirado-Rives, W.L. Jorgensen, 1.14*CM1A-LBCC: localized Bond-charge corrected CM1A charges for condensed-phase simulations, J. Phys. Chem. B 121 (2017) 3864–3870, https://doi.org/10.1021/acs.jpcb.7b00272.
[74] L.S. Dodda, I.C. De Vaca, J. Tirado-Rives, W.L. Jorgensen, LigParGen web server: an automatic OPLS-AA parameter generator for organic ligands, Nucleic Acids Res. 45 (2017) W331–W336, https://doi.org/10.1093/NAR/GKX312.
[75] J. Huang, A.D. Mackerell, CHARMM36 all-atom additive protein force field: validation based on comparison to NMR data, J. Comput. Chem. 34 (2013) 2135–2145, https://doi.org/10.1002/JCC.23354.
[76] W.L. Jorgensen, J. Chandrasekhar, J.D. Madura, R.W. Impey, M.L. Klein, Comparison of simple potential functions for simulating liquid water, J. Chem. Phys. 79 (1983) 926–935, https://doi.org/10.1063/1.445869.
[77] A.D. MacKerell, D. Bashford, M. Bellott, R.L. Dunbrack, J.D. Evanseck, M.J. Field, S. Fischer, J. Gao, H. Guo, S. Ha, D. Joseph-McCarthy, L. Kuchnir, K. Kuczera, F.T. K. Lau, C. Mattos, S. Michnick, T. Ngo, D.T. Nguyen, B. Prodhom, W.E. Reiher, B. Roux, M. Schlenkrich, J.C. Smith, R. Stote, J. Straub, M. Watanabe,

J. Wiórkiewicz-Kuczera, D. Yin, M. Karplus, All-atom empirical potential for molecular modeling and dynamics studies of proteins, J. Phys. Chem. B 102 (1998) 3586–3616, https://doi.org/10.1021/jp973084f.
[78] J.A. Lemkul, From proteins to perturbed Hamiltonians: a suite of tutorials for the GROMACS-2018 molecular simulation package [article v1.0], Living J Comput Mol Sci 1 (2019) 5068, https://doi.org/10.33011/LIVECOMS.1.1.5068.
[79] E.F. Pettersen, T.D. Goddard, C.C. Huang, G.S. Couch, D.M. Greenblatt, E.C. Meng, T.E. Ferrin, UCSF chimera—a visualization system for exploratory research and analysis, J. Comput. Chem. 25 (2004) 1605–1612, https://doi.org/10.1002/JCC.20084.
[80] T.D. Goddard, C.C. Huang, E.C. Meng, E.F. Pettersen, G.S. Couch, J.H. Morris, T. E. Ferrin, UCSF chimerax: meeting modern challenges in visualization and analysis, Protein Sci. 27 (2018) 14–25, https://doi.org/10.1002/PRO.3235.
[81] E.F. Pettersen, T.D. Goddard, C.C. Huang, E.C. Meng, G.S. Couch, T.I. Croll, J. H. Morris, T.E. Ferrin, UCSF chimerax: structure visualization for researchers, educators, and developers, Protein Sci. 30 (2021) 70–82, https://doi.org/10.1002/PRO.3943.
[82] Y. Xie, H. Li, X. Luo, H. Li, Q. Gao, L. Zhang, Y. Teng, Q. Zhao, Z. Zuo, J. Ren, IBS 2.0: an upgraded illustrator for the visualization of biological sequences, Nucleic Acids Res. 50 (2022) W420–W426, https://doi.org/10.1093/NAR/GKAC373.